



<b>Title</b>	Properties of giant molecular clouds in the strongly barred galaxy NGC 1300
<b>Author(s)</b>	Maeda, Fumiya; Ohta, Kouji; Fujimoto, Yusuke; Habe, Asao
<b>Citation</b>	Monthly notices of the royal astronomical society, 493(4), 5045-5061 <a href="https://doi.org/10.1093/mnras/staa556">https://doi.org/10.1093/mnras/staa556</a>
<b>Issue Date</b>	2020-04
<b>Doc URL</b>	<a href="http://hdl.handle.net/2115/78945">http://hdl.handle.net/2115/78945</a>
<b>Rights</b>	This article has been accepted for publication in Monthly notices of the royal astronomical society ©:2020 Published by Oxford University Press on behalf of The Royal Astronomical Society. All rights reserved.
<b>Type</b>	article
<b>File Information</b>	Mon. Not. Roy. Astron. Soc.493-4_5045-5061.pdf



[Instructions for use](#)

# Properties of giant molecular clouds in the strongly barred galaxy NGC 1300

Fumiya Maeda <sup>1</sup>★, Kouji Ohta,<sup>1</sup> Yusuke Fujimoto <sup>2,3</sup> and Asao Habe<sup>4</sup>

<sup>1</sup>Department of Astronomy, Kyoto University, Kitashirakawa-Oiwake-Cho, Sakyo-ku, Kyoto, Kyoto 606-8502, Japan

<sup>2</sup>Research School of Astronomy & Astrophysics, Australian National University, Canberra, ACT 2611, Australia

<sup>3</sup>Department of Terrestrial Magnetism, Carnegie Institution for Science, 5241 Broad Branch Road NW, Washington, DC 20015, USA

<sup>4</sup>Graduate School of Science, Hokkaido University, Kita 10 Nishi 8, Kita-ku, Sapporo, Hokkaido 060-0810, Japan

Accepted 2020 February 19. Received 2020 February 19; in original form 2019 November 5

## ABSTRACT

Star formation activity depends on galactic-scale environments. To understand the variations in star formation activity, comparing the properties of giant molecular clouds (GMCs) among environments with different star formation efficiency (SFE) is necessary. We thus focus on a strongly barred galaxy to investigate the impact of the galactic environment on the GMC properties, because the SFE is clearly lower in bar regions than in arm regions. In this paper, we present the  $^{12}\text{CO}(1-0)$  observations towards the western bar, arm, and bar-end regions of the strongly barred galaxy NGC 1300 with ALMA 12-m array at a high angular resolution of  $\sim 40$  pc. We detected GMCs associated with the dark lanes not only in the arm and bar-end regions but also in the bar region, where massive star formation is not seen. Using the CPROPS algorithm, we identified and characterized 233 GMCs across the observed regions. Based on the Kolmogorov–Smirnov test, we find that there is virtually no significant variations in GMC properties (e.g. radius, velocity dispersion, molecular gas mass, and virial parameter) among the bar, arm, and bar-end region. These results suggest that systematic differences in the physical properties of the GMCs are not the cause for SFE differences with environments, and that there should be other mechanisms which control the SFE of the GMCs such as fast cloud–cloud collisions in NGC 1300.

**Key words:** ISM: clouds – galaxies: individual: NGC1300 – galaxies: star formation.

## 1 INTRODUCTION

It is important to investigate the relation between star formation rate (SFR) and gas density in the context of galaxy evolution. This relation describes how efficiently galaxies convert their gases into stars. Previous studies on the Milky Way and nearby disc galaxies show that there is a tight correlation between the SFR and the surface density of molecular gas;  $\Sigma_{\text{SFR}} \propto \Sigma_{\text{H}_2}^N$ , where the index  $N$  is between 1 and 2 (e.g. Kennicutt 1998; Bigiel et al. 2008; Schruba et al. 2011). However, variations in the relation have been found; star formation activity changes among galactic-scale environments, and the gas surface density is not the only factor controlling the star formation. Momose et al. (2010) measured the star formation efficiency (SFE =  $\Sigma_{\text{SFR}}/\Sigma_{\text{H}_2}$ ) in a barred galaxy of NGC 4303 at a spatial resolution of 500 pc and reported that the SFEs in the arm regions are about two times higher than those in the bar regions (see also Yajima et al. 2019). Such variations of the SFE with environments are reported for other nearby galaxies and the Milky

Way (e.g. Watanabe et al. 2011; Leroy et al. 2013; Longmore et al. 2013; Hirota et al. 2014; Usero et al. 2015; Gallagher et al. 2018), but physical mechanism which controls the SFE within galaxies is still unclear.

To understand the variation of the SFE, it is important to unveil the properties of giant molecular clouds (GMCs) where star formation occurs. In particular, comparing the GMC properties among environments with different SFEs is necessary. In the Milky Way, GMCs' mass, size, and velocity dispersion are typically  $\sim 10^{4-6} M_{\odot}$ ,  $\sim 20$ – $100$  pc, and  $2$ – $10$  km  $\text{s}^{-1}$ , respectively (e.g. Solomon et al. 1987; Heyer et al. 2009). In recent years, due to high sensitive interferometers, extragalactic GMCs can be observed at a high angular resolution of 20–50 pc; e.g. M51 (Colombo et al. 2014), M83 (Hirota et al. 2018), PHANGS–ALMA survey (A. K. Leroy et al., in prep). For example, Hirota et al. (2018) investigated GMC properties in an intermediate-type barred galaxy of M83 where the SFE in the bar regions is about two times smaller than that in the arm regions. They found the virial parameter, which is a measure for gravitational binding of GMCs, in the bar ( $\sim 1.6$ ) is larger than that in the arm ( $\sim 1.0$ ). This result is consistent with the idea that the many clouds in the bar are gravitationally unbound which makes

\* E-mail: fmaeda@kusastro.kyoto-u.ac.jp

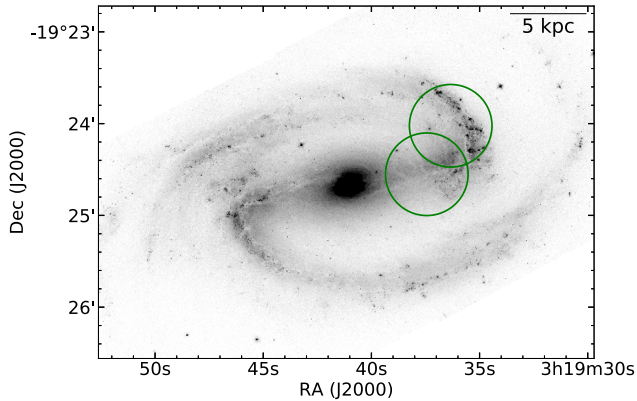


**Figure 1.** V-band image of NGC 1300 taken with *F555W* filter on Advanced Camera for Surveys (ACS) of the *Hubble Space Telescope* (HST). We obtained this image from the Hubble Legacy Archive (<https://hla.stsci.edu/>). The green circles represent fields of view (FoVs; HPBW =  $54'' \phi$ ) observed with ALMA (see Section 2).

the SFE low (see also Egusa et al. 2018). However, only a few such studies on the relation between GMC properties and the variation of star formation activity with environments are made so far.

A strongly barred galaxy is a suitable laboratory for studying the impact of the galactic environments on the GMC properties, because the absence of star formation is clearly seen in bar regions; remarkable dust lane is seen in the bar regions without prominent H II regions, while in the arm regions H II regions are associated with dust lanes. In this study, we therefore focus on a nearby prototype strongly barred galaxy of NGC 1300 (Fig. 1). Maeda et al. (2018) carried out  $^{12}\text{CO}(1-0)$  observations towards the bar and arm regions of NGC 1300 with a single-dish telescope of Nobeyama 45-m telescope. They find that the  $\Sigma_{\text{H}_2}$  in the bar region is comparable to that in the arm region ( $\Sigma_{\text{H}_2} \sim 10 M_{\odot} \text{pc}^{-2}$ ), indicating the star formation activity in the bar region is clearly suppressed.

In this paper, we report  $^{12}\text{CO}(1-0)$  observations towards the western bar, arm, and bar-end regions in NGC 1300 at a high angular resolution of  $\sim 40$  pc with Atacama Large Millimeter/submillimeter Array (ALMA). Our main goals are to measure the properties of GMCs and investigate whether there are differences in the properties with environments. In addition, we compare the properties of GMCs in NGC 1300 with those in a normal spiral galaxy. As pointed out by Hughes et al. (2013), for comparison with different data cubes, it is essential to match the spatial and spectral resolution and line sensitivity to minimize observational bias. In this study, we compare the properties of GMCs in spiral arms of prototype spiral galaxy of M51 by Colombo et al. (2014, C14) because the spatial resolution and line sensitivity are mostly comparable to those of our observations.

This paper is structured as follows: In Section 2, we describe the CO(1-0) observations and data reduction. The resultant CO(1-0) distribution is presented in Section 3. In Section 4, we summarize the method used to identify GMCs. The basic properties of the GMCs and examination of the variations of GMC physical properties with environments are described in Section 5. In Sections 6 and 7, we examine scaling relations and mass spectra of the GMCs. In Section 8, we discuss what physical mechanism controls the SFE of the GMC. Our conclusions are presented in Section 9. We discuss the reliability of the measurements of the GMC properties in Appendix A. The catalogue of GMCs we identified is presented in Appendix B. Table 1 summarizes parameters of NGC 1300 adopted throughout this paper.

**Table 1.** Adopted parameters of NGC 1300.

Parameter	Value
Morphology <sup>a</sup>	SB(s)bc
Centre position (J2000.0) <sup>b</sup>	$03^{\text{h}}19^{\text{m}}41^{\text{s}}.036$ $-19^{\circ}24'40''.00$
Inclination <sup>c</sup>	$50.2^{\circ}$
Distance <sup>d</sup>	20.7 Mpc
Linear scale	$100 \text{ pc arcsec}^{-1}$

*Notes.* <sup>a</sup>Sandage & Tammann (1981).

<sup>b</sup>The peak of Fig. 1.

<sup>c</sup>England (1989).

<sup>d</sup>We adopted the systemic velocity with corrections for the Virgo cluster, the Great Attractor, and the Shapley concentration of  $1511 \text{ km s}^{-1}$  (Mould et al. 2000) and the Hubble constant of  $73 \text{ km s}^{-1} \text{ Mpc}^{-1}$ .

## 2 OBSERVATIONS AND DATA REDUCTION

We carried out  $^{12}\text{CO}(1-0)$  line observations of NGC 1300 on 2017 December 30 and 2018 January 6, 7, 13, and 16 with ALMA (program ID: 2017.1.00248.S, PI = F. Maeda). To cover the regions observed with  $^{12}\text{CO}(1-0)$  by Maeda et al. (2018), two pointings were centred at (RA, Dec.) = ( $3^{\text{h}}19^{\text{m}}37^{\text{s}}.435$ ,  $-19^{\circ}24'33''.24$ ) and ( $3^{\text{h}}19^{\text{m}}36^{\text{s}}.326$ ,  $-19^{\circ}24'01''.42$ ) in J2000 as shown with the green circles in Fig. 1. The ALMA primary beam for the 12-m array is  $54 \text{ arcsec}$  at HPBW.

The ALMA observations were taken during five separated periods with seven execution blocks in total. Table 2 summarizes the details of the ALMA observations. The total on-source time was 5.31 h (2.65 h for each position). For all observations, we used about 44 antennas with C43-5 configuration. The projected baseline length ranged from 15.1 m to 2.5 km, which corresponds to a maximum recoverable scale of  $\sim 21.4 \text{ arcsec}$  at 115 GHz. We used the Band 3 receiver with the central frequency of 114.664 GHz, channel width of 244.1 kHz ( $\sim 0.64 \text{ km s}^{-1}$ ), and bandwidth of 468.8 MHz ( $\sim 1225 \text{ km s}^{-1}$ ). Bandpass and phase were calibrated with J0423-0120 and J0340-2119, respectively. J0423-0120 was also used as a flux calibrator. The  $T_{\text{sys}}$  and PWV were typically 100–150 K and 1–5 mm during the observations, respectively.

We calibrated raw visibility data using the Common Astronomy Software Applications (CASA) ver. 5.1.1. and the observatory-provided calibration script. We reconstructed the two-field mosaic image using CASA ver. 5.4.0. First, we combined the calibrated visibility data of the two pointing positions using `concat` task. Then, we imaged the concatenated visibility using the multi-scale CLEAN algorithm (Cornwell 2008), which models an image by a collection of multiple Gaussians with different full width at half-maximum (FWHM) values. As shown by Rich et al. (2008), this method works well in reducing the depth of negative emission features (so-called negative bowl) and recovering extended emission in comparison to the standard CLEAN algorithm, which models an image by a collection of point sources. We used the task `tclean` for imaging by adopting the factors of 1, 2, and 5 times the synthesized beam as multiscale parameter and Briggs weighting with `robust = 0.5`. To ensure consistency with C14 and to achieve a reasonable S/N, we choose a velocity resolution of  $5 \text{ km s}^{-1}$  and a pixel size of  $0.12 \text{ arcsec}$ . The resultant rms noise is  $0.51 \text{ mJy beam}^{-1}$ , corresponding to  $0.36 \text{ K}$ . Finally, we applied the primary beam correction on the output restored image. In this study, we used the region within the primary beam correction factor smaller than 2.0. The final data cube has an angular resolution of  $0.44 \text{ arcsec} \times 0.30 \text{ arcsec}$ .

**Table 2.** Observation settings.

Execution block	Start time (UTC)	On-source time (min)	Number of antennas	Baseline range
uid___A002_Xc889b6_X21a3.ms	2017/12/30 02:27:10	45.55	46	15.1 m–2.5 km
uid___A002_Xc889b6_X2691.ms	2017/12/30 03:36:38	45.53	46	15.1 m–2.5 km
uid___A002_Xc8d560_X4fa.ms	2018/01/06 23:17:13	45.55	44	15.1 m–2.5 km
uid___A002_Xc8d560_X9e4.ms	2018/01/07 00:26:35	45.48	44	15.1 m–2.5 km
uid___A002_Xc8d560_X9737.ms	2018/01/07 22:10:49	45.50	43	15.1 m–2.5 km
uid___A002_Xc91189_X727.ms	2018/01/13 01:59:20	45.52	44	15.1 m–2.5 km
uid___A002_Xc92fe3_X8e21.ms	2018/01/16 22:21:23	45.50	44	15.1 m–1.4 km

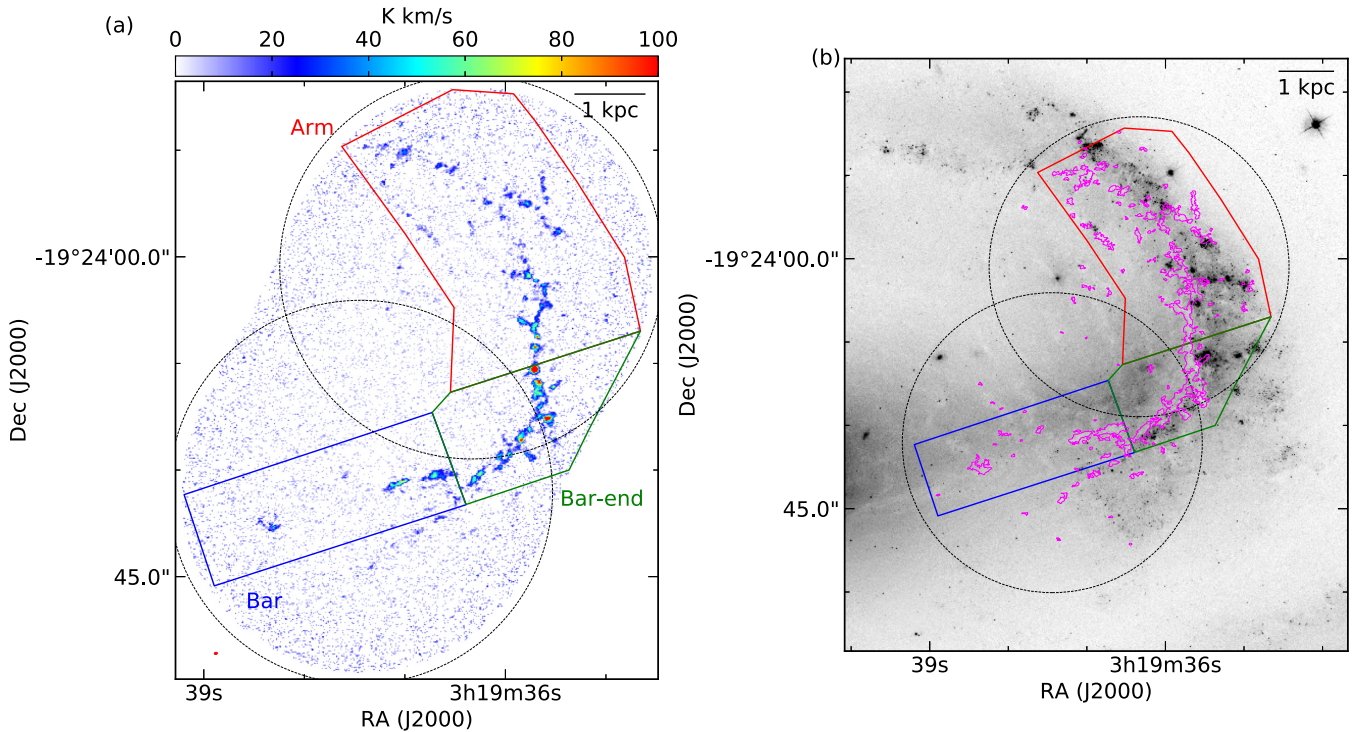


**Figure 2.** (a) Velocity-integrated intensity  $^{12}\text{CO}(1-0)$  image of NGC 1300 generated from the ALMA data cube. We used channel maps within the velocity range  $1540\text{--}1690\text{ km s}^{-1}$  clipped at  $3\sigma$  ( $1.53\text{ mJy beam}^{-1}$ ). The black dotted circles ( $54''\phi$ ) represent FoV observed with ALMA. The colour solid lines indicate the definition of the environmental mask. *Bar*, *arm*, and *bar-end* are indicated with blue, red, and green lines, respectively. (b) CO contours in magenta are superimposed on the  $F555W$  image obtained from *HST* archive data. CO contours are created from the significant emission identified by CPROPS. The contour level of the CO map is  $8.0\text{ K km s}^{-1}$ .

### 3 GMC SCALE MOLECULAR GAS DISTRIBUTION IN NGC 1300

Fig. 2(a) shows a map of the velocity-integrated intensity ( $I_{\text{CO}}$ ). This map is created from channel maps within the LSR velocity range  $1540\text{--}1690\text{ km s}^{-1}$  clipped at  $3\sigma$  ( $= 1.53\text{ mJy beam}^{-1}$ ). The clipping is only for visualization purpose. We detected  $^{12}\text{CO}(1-0)$  emission from the western arm to the bar region. Due to the high angular resolution of  $\sim 40\text{ pc}$ , the CO emission is resolved into GMC scale. Fig. 2(b) compares the CO distribution with the map of H II regions and dust lanes. The grey-scale image is the V-band image (same as Fig. 1). The magenta contours in Fig. 2(b) show the CO emission with  $8.0\text{ K km s}^{-1}$ . These contours are created from the significant emission identified by CPROPS (so-called island regions; see Section 4.1).

In this study, to compare physical properties of GMCs among galactic environments, we separated NGC 1300 into *bar*, *arm*, and *bar-end* regions, according to Fig. 2. The blue rectangle is defined

as the *bar* region, which covers the dark lane and associated spurs that are connected almost perpendicularly to the dark lane. The *arm* region is defined as a red polygon. The green polygon that covers the intersection region of the bar and the arm is defined as the *bar-end* region. These colour codes will be kept throughout this paper. The deprojected area is  $5.1$ ,  $9.9$ , and  $3.6\text{ kpc}^2$  in *bar*, *arm*, and *bar-end*, respectively.

Here, we see the feature of the CO emissions in each region. In *arm* and *bar-end*, the mean  $I_{\text{CO}}$  within the region we detected significant emission is  $20$  and  $32\text{ K km s}^{-1}$  in *arm* and *bar-end*, respectively. These values correspond to  $55$  and  $90\text{ M}_{\odot}\text{ pc}^{-2}$  assuming the standard CO-to- $\text{H}_2$  conversion factor ( $\alpha_{\text{CO}}$ ) of  $4.4\text{ M}_{\odot}(\text{K km s}^{-1}\text{ pc}^2)^{-1}$ . In these regions, most of CO emissions are associated with  $\text{H}\alpha$  emissions and coexist with dust lanes. This good correspondence of the CO emissions to the dust lanes and displacement of the  $\text{H}\alpha$  and CO emissions are often seen in spiral galaxies at a high angular resolution of  $\sim 50\text{ pc}$  (e.g. M51; Schinnerer et al. 2013). This is naturally interpreted with respect

to the spiral density wave; the gases go into the spiral density wave, then dense shocked gas regions form in the spiral arms which result in the formation of GMCs. In the GMCs, stars form, and massive stars born produce H II regions. The stellar feedback (e.g. stellar wind, supernova) would disperse the molecular gas, thus contributing to the observed offset.

In *bar*, we detected GMC-like CO emissions on the dust lanes. The mean  $I_{\text{CO}}$  is  $22 \text{ K km s}^{-1}$ , corresponding to  $60 \text{ M}_{\odot} \text{ pc}^{-2}$ . Unlike *arm*, however, no prominent H II region is associated with the CO emissions. This result indicates that massive star formation in the bar region of the strongly barred galaxy is suppressed despite the presence of GMC-like molecular gases. Note that we did not detect significant CO emission above  $4\sigma$  of  $T_{\text{peak}} = 1.44 \text{ K}$ , corresponding to an average surface density of  $20 \text{ M}_{\odot} \text{ pc}^{-2}$  for a single pixel and spectral channel, in part of the dust lane in the bar region.

## 4 GMC IDENTIFICATION AND CHARACTERIZATION

### 4.1 GMCs identification

The choice of an algorithm for identifying GMCs can be the largest source of uncertainty in measuring and comparing GMC properties. In this study, we used 3D clumps finding algorithm CPROPS (Rosolowsky & Leroy 2006) which is designed to identify GMCs well even at low sensitivities. The spatial resolution and line sensitivity of our data cube are comparable to those of the data cube of M51 by Schinnerer et al. (2013) which was observed with the Plateau de Bure Interferometer and IRAM 30-m telescope at a spatial resolution of  $\sim 40 \text{ pc}$  and a line sensitivity of  $0.4 \text{ K}$  at  $5 \text{ km s}^{-1}$  bin. Using CPROPS, C14 identified GMCs in M51 from the data cube. Therefore, we adopt almost the same CPROPS parameters adopted in C14 to make a proper comparison and minimize systematics.

Here, we provide a brief summary of CPROPS. CPROPS has been fully described by Rosolowsky & Leroy (2006). This algorithm begins with the identification of regions with significant emissions within the data cube (called the ‘islands’ in CPROPS). CPROPS identifies pixels in which the signal is above  $t\sigma_{\text{rms}}$  in at least two adjacent velocity channels, where  $\sigma_{\text{rms}}$  is the rms noise of the data cube. Since the data cube is corrected for the primary beam pattern, the noise in the map is non-uniform. Thus, we calculated a spatially varying of the rms noise in the map by calling NONUNIFORM flag in CPROPS. CPROPS then grows these regions to include adjacent pixels in which the signal is above  $e\sigma_{\text{rms}}$ . The  $t$  and  $e$  are the THRESHOLD and EDGE parameters in CPROPS, respectively. We chose  $t = 4.0$  and  $e = 1.5$  to ensure consistency with C14.

After the identification of the islands, the islands are divided into individual GMCs using a modified watershed algorithm. CPROPS searches for local maxima within a box of three times the beam and channel width, corresponding to  $\sim 120 \text{ pc} \times 120 \text{ pc} \times 15 \text{ km s}^{-1}$ . All local maxima are required to lie at least  $2\sigma_{\text{rms}}$  above the merge level with another maximum. Only emission that is uniquely associated with each local maximum is given an assignment (i.e. only that emission which is above all merge levels with other local maxima).

For every pair of local maxima in an island, CPROPS compares the values of the moments at contour levels just above and just below the merge level. If the moments jump by more than a user-defined fraction, called SIGDISCONT parameter, the two local maxima are categorized as distinct, otherwise they are merged into a single cloud. The default parameter of SIGDISCONT = 1.0

requires 100 per cent or more fractional change. As described in C14, however, setting of SIGDISCONT > 0.0 does not work well for the CO bright regions where a lot of local maxima are connected at a very low contour level; CPROPS misses objects that visual inspection suggests are GMCs (see Appendix B in C14). In our data cube, some GMCs are missed with SIGDISCONT > 0.0 in bar-end where CO emission is the brightest. To avoid this failure, we set SIGDISCONT to 0.0 which makes no attempt to merge the two local maxima into a single cloud. In other words, each local maximum is assigned to an individual independent cloud. The remainder of the emission is considered to be in the watershed, and CPROPS does not assign it to any cloud.

A large number of objects were found whose peak temperature is above  $4\sigma_{\text{rms}}$  but temperature of the adjacent pixels in the velocity axis is lower than  $4\sigma_{\text{rms}}$ . These objects seem to be GMCs because their size, velocity dispersion, and luminosity are similar to those in M51 spiral arms. However, they are missed by CPROPS because CPROPS does not identify objects which do not contain two consecutive pixels above  $4\sigma_{\text{rms}}$  in the velocity axis. Therefore, to identify such GMCs for which signal above  $4\sigma_{\text{rms}}$  is detected in only a single channel, we allowed CPROPS to identify an island which has pixels above  $4\sigma_{\text{rms}}$  in only one channel. As we will discuss in Section 5, the possibility that these GMCs are spurious is very low.

### 4.2 Derivation of basic properties

#### 4.2.1 Size, velocity width, and CO luminosity

CPROPS determines the size, velocity width, and flux of GMCs using moment methods. CPROPS corrects for the sensitivity by extrapolating GMC properties to those we would expect to measure with perfect sensitivity (i.e. 0 K) and the resolution by deconvolution for the beam and channel width. Details of the measurement method of CPROPS are described in Rosolowsky & Leroy (2006).

The effective radius of the GMC is defined as  $R = (3.4/\sqrt{\pi})\sigma_r$ , where  $\sigma_r$  is geometric mean of the second intensity-weighted moments along the major and minor axis (i.e. rms size) and  $3.4/\sqrt{\pi}$  is an empirical factor defined by Solomon et al. (1987). If the extrapolated rms size is smaller than the beam size of  $15.4 \text{ pc}$ , we set this value as an upper limit of the rms size. The velocity width,  $\sigma_v$ , is computed as the intensity-weighted second moment of the velocity after the deconvolution to correct the velocity resolution ( $\Delta V_{\text{chan}}$ ). CPROPS approximates the shape of the channel as a Gaussian with an integral area equal to that of the channel width (i.e.  $\Delta V_{\text{chan}}/\sqrt{2\pi}$ ). The CO luminosity,  $L_{\text{CO}}$ , is derived from

$$\left(\frac{L_{\text{CO}}}{\text{K km s}^{-1} \text{ pc}^2}\right) = \left(\frac{F_{\text{CO}}}{\text{K km s}^{-1} \text{ arcsec}^2}\right) \left(\frac{D}{\text{pc}}\right)^2 \left(\frac{\pi}{180 \times 3600}\right)^2, \quad (1)$$

where  $F_{\text{CO}}$  is the zeroth moment of the intensity and the  $D$  is the distance to NGC 1300 of  $20.7 \text{ Mpc}$ .

The median ratio of the extrapolated (i.e. without deconvolution) radius and velocity dispersion to the directly measured (i.e. without deconvolution and extrapolation) are 1.5 and 1.4, respectively. For the CO luminosity, the median ratio of the extrapolated value to the directly measured value is 2.1. These correction factors are comparable to those of the GMCs in M51 (C14).

#### 4.2.2 Derived properties

The molecular gas mass of a GMC,  $M_{\text{mol}}$ , is converted from the CO luminosity by adapting an  $\alpha_{\text{CO}}$ :

$$\left(\frac{M_{\text{mol}}}{\text{M}_{\odot}}\right) = \alpha_{\text{CO}} \left(\frac{L_{\text{CO}}}{\text{K km s}^{-1} \text{ pc}^2}\right). \quad (2)$$

We adopt the standard  $\alpha_{\text{CO}}$  of  $4.4 M_{\odot} (\text{K km s}^{-1} \text{pc}^2)^{-1}$  to ensure consistency with C14. Note that this  $\alpha_{\text{CO}}$  includes a factor of 1.36 to account for the presence of helium.

Assuming a spherical GMC with the power-law density profile of  $\rho \propto r^{-n}$ , we calculate the virial mass of a GMC,  $M_{\text{vir}}$ , from the size and velocity dispersion as

$$\begin{aligned} M_{\text{vir}} &= \frac{3(5-2n)}{3-n} \frac{R\sigma_v^2}{G} \\ &= 1040 \left(\frac{R}{\text{pc}}\right) \left(\frac{\sigma_v}{\text{km s}^{-1}}\right)^2 [M_{\odot}]. \end{aligned} \quad (3)$$

We adopt the profile of  $n = 1$  to ensure consistency with previous studies. We assume that magnetic fields and external pressure are negligible.

The average molecular gas surface density,  $\Sigma_{\text{mol}}$ , is defined as

$$\Sigma_{\text{mol}} = \frac{M_{\text{mol}}}{\pi R^2}. \quad (4)$$

The virial parameter,  $\alpha_{\text{vir}}$ , is a useful measure of the gravitational binding and is defined as

$$\alpha_{\text{vir}} = \frac{5\sigma_v^2 R}{GM_{\text{mol}}} \quad (5)$$

by Bertoldi & McKee (1992). This definition assumes  $n = 0$ , but the impact of the difference between  $n = 0$  and 1 is only about 10 per cent. GMCs with  $\alpha_{\text{vir}} \lesssim 2$  are typically considered to be bound. A value of  $\alpha_{\text{vir}} > 2$  indicates that the GMC is gravitationally unbound.

The scaling coefficient,  $c$ , characterizes the scaling between the size and the velocity dispersion of a GMC as

$$c \equiv \frac{\sigma_v}{R^{0.5}}. \quad (6)$$

For a GMC with  $\alpha_{\text{vir}} = 1$ ,  $c$  can be related to the molecular gas surface density as  $c = (\pi G \Sigma_{\text{mol}}/5)^{0.5}$ .

CPROPS estimates the uncertainty of these GMC properties using a bootstrapping method, and the final uncertainty is the standard deviation of the bootstrapped values scaled up by the square root of the oversampling rate. The oversampling rate is equal to the number of pixels per beam, which accounts for the non-independence of the pixels. C14 found that 50 bootstrapping measurements provided a reliable estimation of the uncertainty, thus we adopted this number.

## 5 BASIC PROPERTIES OF GMCs

CPROPS identified 233 GMCs in the data cube. 166 of the GMCs have at least two consecutive pixels above  $4\sigma_{\text{rms}}$  in the velocity axis direction. The remaining 67 GMCs have pixels above  $4\sigma_{\text{rms}}$  in only one channel. Fig. 3 shows GMC distribution in NGC 1300. We detected 34, 119, and 49 GMCs in *bar*, *arm*, and *bar-end*, respectively. 31 GMCs are outside the three regions (i.e. in interarm regions). The GMC catalogue in NGC 1300 is presented in Appendix B, which is available in machine-readable form in the online journal.

We inspected the CO line profiles from each GMC CPROPS identified visually, and an obvious spurious signal was not found. To check contamination by spurious sources, we counted the number of local maxima in the data cube scaled by  $-1$  with the same settings described in Section 4.1. We found no false positives which have two consecutive pixels above  $4\sigma_{\text{rms}}$  in the velocity axis direction. For the 166 GMCs, we therefore believe there is no contamination by spurious sources. On the other hand, CPROPS identified three false

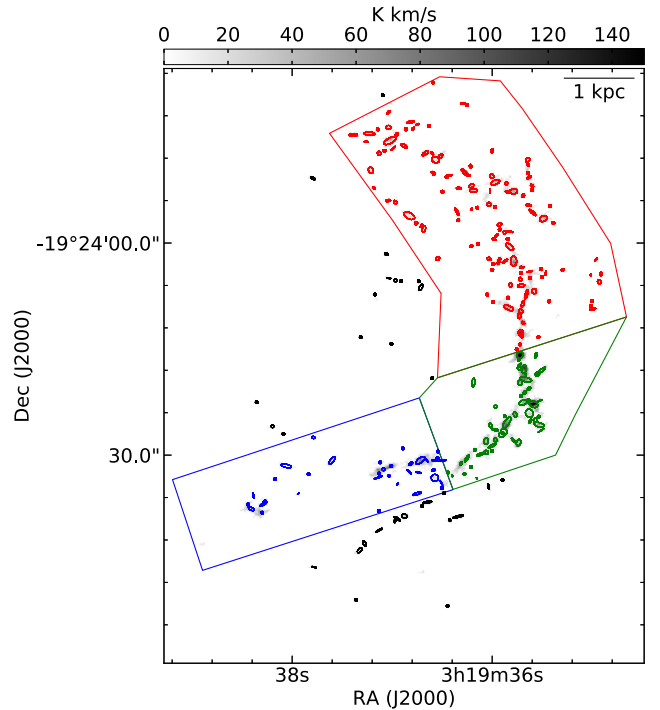


**Figure 3.** GMC distribution in NGC 1300 superimposed on the velocity-integrated CO map (grey-scale). The GMCs are represented as ellipses with the extrapolated and deconvolved major and minor axes, oriented according to the measured position angle. The colours indicate the environment defined in Fig. 2.

positives which have pixels above  $4\sigma_{\text{rms}}$  in only one channel. Thus,  $\sim 3$  of the 67 ( $\sim 4$  per cent) GMCs for which signal above  $4\sigma_{\text{rms}}$  is detected in only a single channel are expected to be spurious.

With the adopted parameters for CPROPS, GMCs with  $T_{\text{peak}} > 4\sigma_{\text{rms}}$ , which corresponds to  $\sim 1.44$  K, were detected. The mass completeness limit is estimated to be  $2.0 \times 10^5 M_{\odot}$  by assuming that a minimum detectable GMC has a size and a velocity width comparable to the beam size and the channel width, respectively, and  $\alpha_{\text{CO}}$  is  $4.4 M_{\odot} (\text{K km s}^{-1} \text{pc}^2)^{-1}$ . We find that 154 of these 233 GMCs are resolved by the synthesized beam. When the observed size is similar to the beam size, uncertainties of  $R$  are greatly magnified by the deconvolution process (e.g. Faesi, Lada & Forbrich 2018). Fig. 4 shows the ratio of directly measured radius to the corrected radius (i.e. with extrapolation and deconvolution) as a function of the corrected radius. Below 15 pc ( $\log R = 1.17$ ), the ratio is often larger than a factor of 2, or even higher. Further, we find only 47 per cent of the GMCs with  $M_{\text{mol}} < 5.0 \times 10^5 M_{\odot}$  are resolved, while 95 per cent of the GMCs with  $M_{\text{mol}} \geq 5.0 \times 10^5 M_{\odot}$  are resolved. Therefore, we defined the GMCs with  $M_{\text{mol}} \geq 5.0 \times 10^5 M_{\odot}$  and  $R > 15$  pc as a resolved sample for the investigation of  $R$ ,  $M_{\text{vir}}$ ,  $\Sigma_{\text{mol}}$ ,  $\alpha_{\text{vir}}$ , and  $c$ , and defined the GMCs with  $M_{\text{mol}} > 2.0 \times 10^5 M_{\odot}$  as a mass completed sample for the investigation of  $T_{\text{peak}}$ ,  $\sigma_v$ , and  $M_{\text{mol}}$ .

### 5.1 Variation of GMC physical properties with environment

Fig. 5 shows the distribution of GMC properties. We use a box and whiskers plot as C14 used for M51. In this plot, the ends of the box represent the upper and lower quartiles ( $Q_1$  and  $Q_3$ , respectively). The median value or  $Q_2$  is marked by a vertical line in the box. The upper whisker expands to the largest data point below  $Q_3 + 1.5\Delta Q$

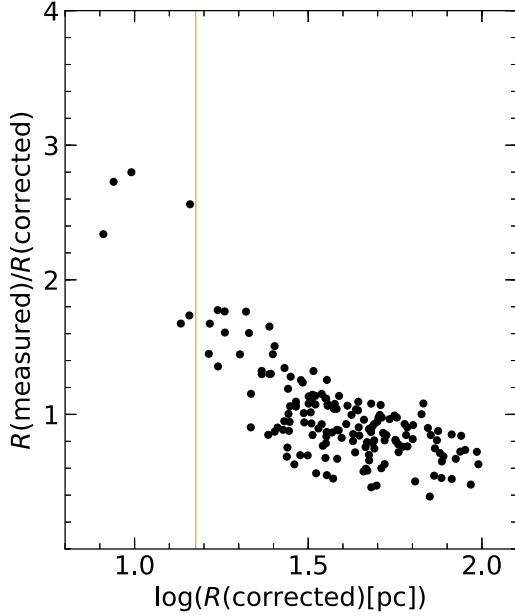


**Figure 4.** Ratio of measured radius to corrected (i.e. with deconvolution and extrapolation) radius for all resolved GMCs against corrected radius. The vertical orange line indicates 15 pc.

and the lower whisker expands to the smallest data point above  $Q_1 - 1.5\Delta Q$ , where  $\Delta Q$  is the box length or  $Q_3 - Q_1$ . For a Gaussian distribution, the region within the whiskers contains 99.3 per cent ( $\pm 2.7\sigma$ ) of the population. The data points outside the whiskers are considered to be outliers. Except for  $T_{\text{peak}}$ ,  $\sigma_v$ , and  $M_{\text{mol}}$ , we show a box and whiskers plot for the resolved sample. The orange lines and bands in Fig. 5 show the median value and the range from  $Q_1$  to  $Q_3$  of those in M51 spiral arms from the catalogue of C14. The median value and the range from  $Q_1$  to  $Q_3$  of each physical property are listed in Table 3.

We investigated the environmental variation of GMC properties in NGC 1300 and compared to the GMC properties in M51 spiral arms. We used the two-sided Kolmogorov–Smirnov (K-S) test to statistically evaluate differences in GMC property distributions for different environments in NGC 1300. We used `stats.kstest2samp` function of python’s SCIPY package, which calculates  $p$ -value based on the approximately formula given by Stephens (1970). To estimate the uncertainties of the  $p$ -values, we made resampling with 100 realizations. In one realization, random values of a given property were generated within the bootstrap uncertainties CPROPS calculated. The most likely  $p$ -value and its uncertainty are the median and the median absolute deviation (MAD) of 100 realizations, respectively. Table 4 shows the results for each GMC physical parameter. Since CPROPS does not provide uncertainties of the  $T_{\text{peak}}$ , we applied rms noise of the data cube, 0.36 K as the uncertainty. We also show the  $p$ -value for the observed value in parentheses. Following the conventional criteria, the two cumulative distribution functions are considered to be significantly different if the  $p$ -value is less than 0.01. A  $p$ -value within 0.01 to 0.05 indicates that the difference is marginally significant. Note that the approximation of  $p$ -value is quite good for  $N_1N_2/(N_1 + N_2) \geq 4$ , where  $N_1$  and  $N_2$  are the number of data points in the first and second distribution, respectively (Stephens 1970). Our sample sufficiently meets this criterion,  $N_1N_2/(N_1 + N_2) \geq 8$ .

**Peak temperature** (Fig. 5a): The  $T_{\text{peak}}$  in *bar-end* is the highest (2.8–4.3 K), followed by *arm* (2.2–3.4 K) and *bar* (2.0–2.4 K).

The K-S test indicates that the differences between *bar-end* and *arm* or *bar* are significant, and that between *bar* and *arm* is marginally significant. Thus, we conclude that the  $T_{\text{peak}}$  in *bar-end* is significantly higher than those in *arm* and *bar*. This result does not change for the resolved sample. The  $\Delta Q$  of  $T_{\text{peak}}$  distribution in *arm* and *bar-end* is within that in M51 spiral arm, but that in *bar* is lower.

**Velocity dispersion** (Fig. 5b): We find no environmental variations based on the K-S test: 4.8–6.5 km s<sup>-1</sup> in *bar*, 4.2–6.5 km s<sup>-1</sup> in *arm*, and 4.7–7.6 km s<sup>-1</sup> in *bar-end*. In *bar-end*, some GMCs have a  $\sigma_v$  larger than 10 km s<sup>-1</sup>. The  $\Delta Q$  of  $\sigma_v$  distribution in each region is roughly within those in M51 spiral arm. One caveat of measurement of  $\sigma_v$  is that we may overestimate  $\sigma_v$  of GMCs. We discuss this bias in Section 5.2 and Appendix A.

**Radius** (Fig. 5c): There are no environmental variations of  $R$  (31.3–64.5 pc in *bar*, 36.7–57.5 pc in *arm*, and 37.1–67.0 pc in *bar-end*) and the  $\Delta Q$  of  $R$  distribution in each region is roughly within those in M51 spiral arms. Note that we evaluate differences in radius without deconvolution for all sample using the K-S test, and we find no environmental variations.

**Molecular gas mass** (Fig. 5d): Molecular gas mass is proportional to a combination of brightness temperature, velocity dispersion, and size:  $M_{\text{mol}} \propto L_{\text{CO}} \propto \langle T \rangle R^2 \sigma_v$ , where  $\langle T \rangle$  is an average brightness temperature. Since the  $R$  and  $\sigma_v$  are roughly equal in each region,  $M_{\text{mol}}$  is mainly proportional to  $\langle T \rangle$  in NGC 1300. Therefore,  $M_{\text{mol}}$  in *bar-end* is expected to be larger than those in *arm* and *bar* like the  $T_{\text{peak}}$ . In fact, the  $M_{\text{mol}}$  in *bar-end* is higher ( $(5.0\text{--}15.5) \times 10^5 M_{\odot}$ ) than those in *bar* ( $(3.7\text{--}8.2) \times 10^5 M_{\odot}$ ) and *arm* ( $(3.4\text{--}9.7) \times 10^5 M_{\odot}$ ). The median value in *bar-end* is by a factor of 1.6 larger than those in *bar* and *arm*. The K-S test indicates that the difference between *bar-end* and *arm* (*bar*) is significant (marginally significant), and there is no significant difference between *bar* and *arm*. The median  $M_{\text{mol}}$  in *bar-end* is comparable to that in M51 spiral arms, but those in *arm* and *bar* are about two times lower.

**Virial mass** (Fig. 5e): Since the  $R$  and  $\sigma_v$  are roughly equal in each region,  $M_{\text{vir}} \propto R\sigma_v^2$  is expected to be equal. In fact, we find no significant environmental variation:  $(1.1 \times -2.3) \times 10^6 M_{\odot}$  in *bar*,  $(1.0 \times -2.1) \times 10^6 M_{\odot}$  in *arm*, and  $(1.2 \times -3.1) \times 10^6 M_{\odot}$  in *bar-end*.

**Molecular gas surface density** (Fig. 5f): Because  $S_{\text{mol}}$  is proportional to  $\langle T \rangle \sigma_v$ ,  $S_{\text{mol}}$  is expected to show the same tendency as  $T_{\text{peak}}$ . In fact,  $S_{\text{mol}}$  in *bar-end* is the highest (138.5–317.6  $M_{\odot} \text{pc}^{-2}$ ), followed by *arm* (112.0–214.8  $M_{\odot} \text{pc}^{-2}$ ) and *bar* (88.8–213.4  $M_{\odot} \text{pc}^{-2}$ ). Based on K-S test, however, we do not find the significant difference.

**Virial parameter** (Fig. 5g): Because  $\alpha_{\text{vir}}$  is proportional to  $\sigma_v/(\langle T \rangle R)$ ,  $\alpha_{\text{vir}}$  is expected to show a reverse tendency of  $T_{\text{peak}}$ . In fact,  $\alpha_{\text{vir}}$  in *bar* is the highest (1.3–2.9), followed by *arm* (1.0–2.1) and *bar-end* (0.9–2.2). Based on the resampling method,  $58 \pm 8$  per cent of the GMCs in *bar* is gravitationally unbound ( $\alpha_{\text{vir}} > 2$ ). This percentage is larger than that in *arm* and *bar-end* ( $33 \pm 4$  per cent and  $29 \pm 3$  per cent), and in M51 spiral arm (35 per cent). However, the K-S test gives high  $p$ -value which indicates there is no significant environmental variation in  $\alpha_{\text{vir}}$ . Note that the K-S test for the observed value shows the marginally significant difference between *arm* and *bar*. But based on the resampling method, it is rare that K-S test gives a  $p$ -value less than or equal to 0.05. In conclusion, there is no significant environmental variations in  $\alpha_{\text{vir}}$  in NGC 1300.

**Scaling coefficient** (Fig. 5h): As expected from the fact that  $c = \sigma_v/R^{0.5}$  is a combination of  $\sigma_v$  and  $R$ , we find no environmental

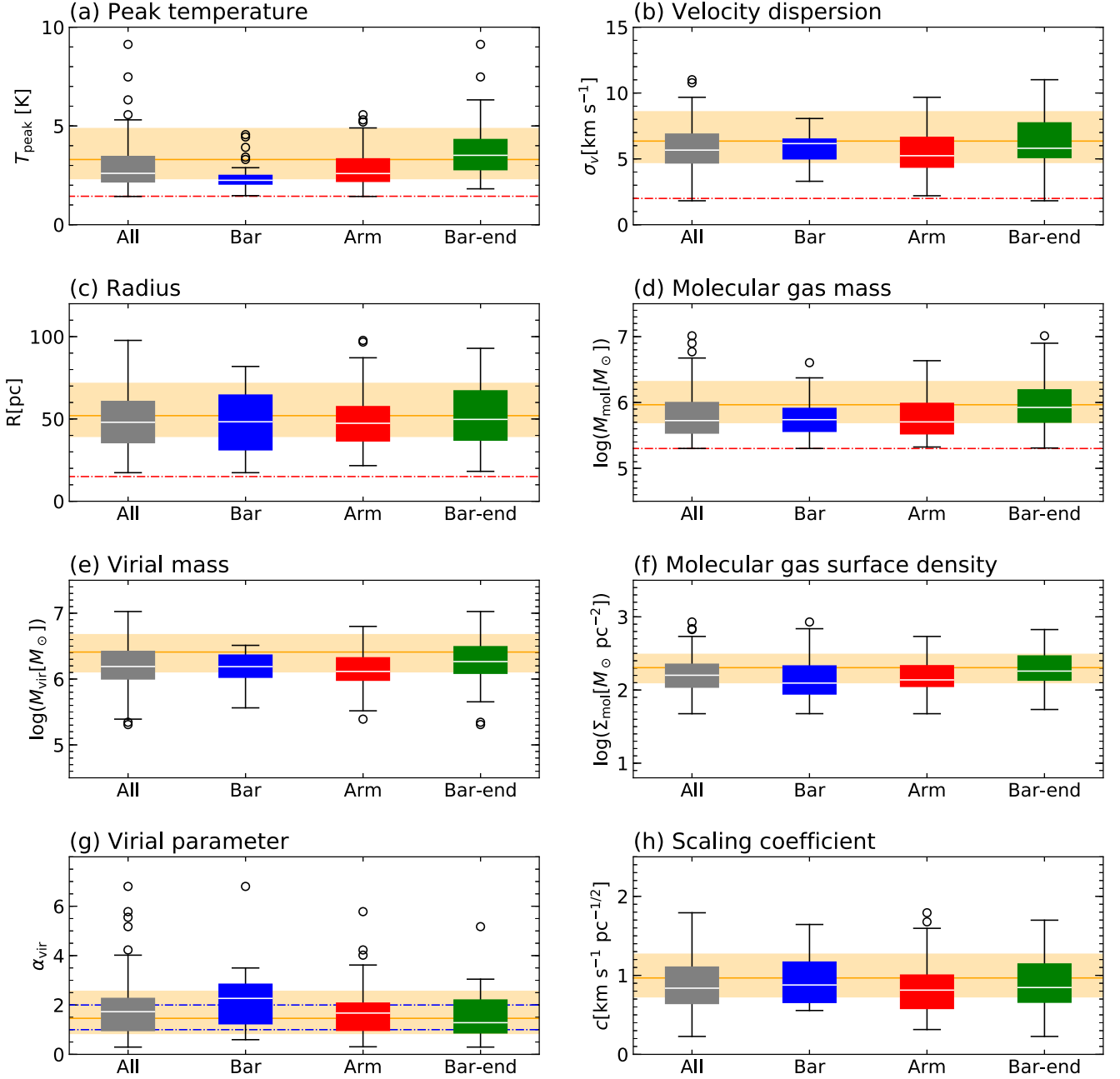


**Figure 5.** Box-and-whisker plots for GMC’s (a) peak temperature ( $T_{\text{peak}}$ ), (b) velocity dispersion ( $\sigma_v$ ), (c) radius ( $R$ ), (d) molecular gas mass ( $M_{\text{mol}}$ ), (e) virial mass ( $M_{\text{vir}}$ ), (f) molecular gas surface density ( $\Sigma_{\text{mol}}$ ), (g) virial parameter ( $\alpha_{\text{vir}}$ ), and (h) scaling coefficient ( $c$ ) in the whole region (grey) and each environment (*bar*: blue, *arm*: red, and *bar-end*: green) of NGC 1300. We used the GMCs with  $M_{\text{mol}} \geq 2.0 \times 10^5 M_{\odot}$  for  $T_{\text{peak}}$ ,  $\sigma_v$ , and  $M_{\text{mol}}$  and the GMCs with  $M_{\text{mol}} \geq 5.0 \times 10^5 M_{\odot}$  and  $R \geq 15$  pc for other properties. The median value is represented as a white horizontal line within each box. Upper and lower edges of each box indicate the upper and lower quartile, respectively ( $Q_1$  and  $Q_3$ , respectively). The upper whisker expands to the largest data point below  $Q_3 + 1.5\Delta Q$  and the lower whisker expands to the smallest data point above  $Q_1 - 1.5\Delta Q$ . The data points outside the whiskers are considered outliers and shown as open circles. The orange solid line and bands show the median value and the range from  $Q_1$  to  $Q_3$  of each property of GMCs in M51 spiral arms (C14). The horizontal red dash-dotted lines indicate 1.44 K ( $=4\sigma$ ),  $2.0 \text{ km s}^{-1}$  ( $=\Delta V_{\text{chan}}/\sqrt{2\pi}$ ), 15 pc, and  $2.0 \times 10^5 M_{\odot}$ . The horizontal blue dash-dotted lines in panel (g) indicate  $\alpha_{\text{vir}} = 1.0$  and  $2.0$ .

variation in  $c$ . The  $c$  in NGC 1300 is comparable to that in M51 spiral arms.

In summary, there is a significant environmental variation in the  $T_{\text{peak}}$ ; the highest value in *bar-end* followed by *arm* and *bar*. Since  $\sigma_v$  and  $R$  do not exhibit environmental variation, the variation of  $T_{\text{peak}}$  is mainly responsible for the variation of median value of  $M_{\text{mol}}$ ,  $\Sigma_{\text{mol}}$ , and  $\alpha_{\text{vir}}$ . But based on the two-sided K-S

tests, the (marginally) significant differences are only seen in the distribution of  $M_{\text{mol}}$  between *bar* and *bar-end*, and *arm* and *bar-end*; there is virtually no significant difference in GMC physical properties among the *bar*, *arm* and *bar-end*. In addition, we find the properties of GMCs in NGC 1300 are roughly comparable to those in M51 spiral arms. In particular, the properties in *bar-end* are very similar.

**Table 3.** GMC properties in the different environments of NGC 1300.

Envir.	Area (kpc <sup>2</sup> )	# <sup>a</sup>	$T_{\text{peak}}^b$ (K)	$\sigma_v^b$ (km s <sup>-1</sup> )	$R^c$ (pc)	$M_{\text{mol}}^b$ (10 <sup>5</sup> M <sub>⊙</sub> )	$M_{\text{vir}}^c$ (10 <sup>5</sup> M <sub>⊙</sub> )	$\Sigma_{\text{mol}}^c$ (M <sub>⊙</sub> pc <sup>-2</sup> )	$\alpha_{\text{vir}}^c$	$c^c$ (km s <sup>-1</sup> pc <sup>-0.5</sup> )
All	37.9	203(104)	2.6 <sup>+0.9</sup> <sub>-0.4</sub>	5.2 <sup>+1.3</sup> <sub>-0.8</sub>	48.0 <sup>+12.6</sup> <sub>-12.4</sub>	5.3 <sup>+4.7</sup> <sub>-1.9</sub>	15.5 <sup>+10.7</sup> <sub>-5.5</sub>	159.2 <sup>+65.9</sup> <sub>-49.7</sub>	1.7 <sup>+0.5</sup> <sub>-0.8</sub>	0.8 <sup>+0.3</sup> <sub>-0.2</sub>
Bar	5.1	28(12)	2.2 <sup>+0.2</sup> <sub>-0.2</sub>	5.7 <sup>+0.8</sup> <sub>-0.9</sub>	48.3 <sup>+16.2</sup> <sub>-17.0</sub>	5.5 <sup>+2.7</sup> <sub>-1.8</sub>	15.4 <sup>+7.8</sup> <sub>-4.7</sub>	125.5 <sup>+87.9</sup> <sub>-36.8</sub>	2.3 <sup>+0.6</sup> <sub>-1.0</sub>	0.9 <sup>+0.3</sup> <sub>-0.2</sub>
Arm	9.9	108(55)	2.6 <sup>+0.7</sup> <sub>-0.4</sub>	5.0 <sup>+1.5</sup> <sub>-0.8</sub>	47.4 <sup>+10.1</sup> <sub>-10.7</sub>	5.1 <sup>+4.6</sup> <sub>-1.7</sub>	13.1 <sup>+8.0</sup> <sub>-3.5</sub>	137.5 <sup>+77.3</sup> <sub>-25.5</sub>	1.7 <sup>+0.4</sup> <sub>-0.7</sub>	0.8 <sup>+0.2</sup> <sub>-0.2</sub>
Bar-end	3.6	43(31)	3.5 <sup>+0.8</sup> <sub>-0.7</sub>	5.6 <sup>+2.0</sup> <sub>-0.9</sub>	49.7 <sup>+17.3</sup> <sub>-12.6</sub>	8.4 <sup>+7.1</sup> <sub>-3.4</sub>	18.4 <sup>+12.6</sup> <sub>-6.2</sub>	181.4 <sup>+111.3</sup> <sub>-45.0</sub>	1.3 <sup>+0.9</sup> <sub>-0.4</sub>	0.8 <sup>+0.3</sup> <sub>-0.2</sub>
M51 SA <sup>d</sup>	14.6	584(365)	3.3 <sup>+1.6</sup> <sub>-1.0</sub>	6.3 <sup>+2.3</sup> <sub>-1.7</sub>	52.0 <sup>+20.0</sup> <sub>-13.0</sub>	9.2 <sup>+12.0</sup> <sub>-4.4</sub>	25.7 <sup>+22.6</sup> <sub>-13.1</sub>	202.0 <sup>+111.7</sup> <sub>-78.5</sub>	1.5 <sup>+1.1</sup> <sub>-0.6</sub>	1.0 <sup>+0.3</sup> <sub>-0.2</sub>

Notes. <sup>a</sup>The number of the GMCs with  $M_{\text{mol}} \geq 2.0 \times 10^5 M_{\odot}$ . In parentheses, we show the number of the GMCs with  $M_{\text{mol}} \geq 5.0 \times 10^5 M_{\odot}$  and  $R \geq 15$  pc.

<sup>b</sup>For the GMCs with  $M_{\text{mol}} \geq 2.0 \times 10^5 M_{\odot}$ .

<sup>c</sup>For the GMCs with  $M_{\text{mol}} \geq 5.0 \times 10^5 M_{\odot}$  and  $R \geq 15$  pc.

<sup>d</sup>For M51 spiral arms (SA) (C14). We extract GMCs with the same selection criteria as described in Section 5.

**Table 4.**  $p$ -values of the Kolmogorov–Smirnov test for GMC properties.

Prop.	Bar versus Arm	Bar versus Bar-end	Arm versus Bar-end
$T_{\text{peak}}^a$	0.019 ± 0.013(0.008)	≪0.01(≪ 0.01)	≪0.01(≪ 0.01)
$\sigma_v^a$	0.350 ± 0.186(0.281)	0.756 ± 0.165(0.667)	0.181 ± 0.083(0.142)
$R^b$	0.672 ± 0.167(0.746)	0.726 ± 0.167(0.896)	0.479 ± 0.153(0.552)
$M_{\text{mol}}^a$	0.876 ± 0.074(0.954)	0.027 ± 0.017(0.037)	0.007 ± 0.004(0.004)
$M_{\text{vir}}^b$	0.794 ± 0.148(0.613)	0.545 ± 0.167(0.698)	0.133 ± 0.067(0.117)
$\Sigma_{\text{mol}}^b$	0.588 ± 0.183(0.355)	0.206 ± 0.102(0.221)	0.123 ± 0.068(0.128)
$\alpha_{\text{vir}}^b$	0.183 ± 0.114(0.050)	0.206 ± 0.106(0.172)	0.813 ± 0.135(0.938)
$c^b$	0.655 ± 0.172(0.778)	0.886 ± 0.092(0.978)	0.430 ± 0.130(0.592)

Notes. In parentheses, we show the  $p$ -value for observed values.

<sup>a</sup>For the GMCs with  $M_{\text{mol}} \geq 2.0 \times 10^5 M_{\odot}$ .

<sup>b</sup>For the GMCs with  $M_{\text{mol}} \geq 5.0 \times 10^5 M_{\odot}$  and  $R \geq 15$  pc.

## 5.2 The reliability of the measurements

### 5.2.1 CPROPS bias

As described in Section 4.2.1, the extrapolated (but non-deconvolved)  $R$ ,  $\sigma_v$ , and  $L_{\text{CO}}$  is typically 1.5–2.0 times higher than the directly measured values. The accuracy of the CPROPS correction (i.e. extrapolation and deconvolution) depends on the sensitivity, spatial resolution, and velocity resolution (Rosolowsky & Leroy 2006). In order to assess the reliability of the measurements of GMC properties, we simulated ALMA observation of mock GMCs, which are three-dimensional Gaussian clouds in position–position–velocity space with given masses, sizes, and velocity dispersions, in CASA under the same condition of our observations (Section 2). After reconstructing the image from the simulated visibility, we identify the GMCs using CPROPS with the same parameters described in Section 4 and compare the input and output values. The details of the simulation method and results are described in Appendix A, and we briefly describe the results and discussion here.

We find that the corrected  $\sigma_v$  is overestimated by  $\sim 50$  per cent if the directly measured velocity width,  $2.35\sigma_v$ , is less than half the channel width of 5.0 km s<sup>-1</sup>. Such GMC accounts for 56 per cent, 64 per cent, and 64 per cent in *bar*, *arm*, and *bar-end*, respectively. Therefore, a large number of catalogued GMCs may be overestimated in the  $\sigma_v$  by a factor of  $\sim 1.5$ . The CPROPS algorithm performs relatively well for the measurements of the  $M_{\text{mol}}$  and  $R$  in comparison to  $\sigma_v$ . We find that the corrected  $M_{\text{mol}}$  is mostly equal to the input  $M_{\text{mol}}$  for the GMC with higher S/N ( $7 \leq S/N \leq 10$ ), but the corrected  $M_{\text{mol}}$  is typically underestimated by  $\sim 10$  per cent for the GMC with lower S/N ( $4 \leq S/N < 7$ ). The corrected  $R$  is typically underestimated by  $\sim 20$  per cent and  $\sim 10$  per cent for the GMC with lower S/N and higher S/N, respectively. We retested the

environmental variation of the GMC properties using the catalogue corrected for the over/underestimation factor. As a result of the K-S test,  $p$ -values do not change much (see Table A2). Thus, we concluded that the over/underestimation of the measurements does not influence on the discussion about the environmental variations described in Section 5.1.

### 5.2.2 Impact of the missing flux

Measurements of GMC properties may be affected by the missing flux (e.g. Rosolowsky & Leroy 2006; Pan & Kuno 2017). Our ALMA observations did not recover the total CO(1–0) flux due to the lack of Atacama Compact Array (ACA) measurements. To estimate the recovery fraction of the total CO(1–0) flux, we compared the CO(1–0) flux obtained from ALMA with those from Nobeyama 45-m single-dish telescope by Maeda et al. (2018), which presented single-pointing observations of several regions in NGC 1300. First, we convolved the CO(1–0) data cube to 13.5 arcsec, the beam size of the Nobeyama 45-m telescope at 115 GHz. We then obtained spectra at the pointing positions of the 45-m telescope and measured the recovery fraction (i.e. the ratio of the two flux). We find that the average recovery fraction is 54 per cent with typical uncertainty of 5 per cent; about half of the total flux was missed, which could affect the measurements of GMC properties.

To investigate the relationship between the spatial scale of the gas distribution and missing flux, we simulated ALMA observation of a mock Gaussian component. We created a fits image of a circular Gaussian component with total flux of 1.0 Jy and given FWHM. The FWHM was set from 100 to 1500 pc every 100 pc. In order to extract the effect originated from the uv-distribution, we simulated the observation under the same configuration and noise-free condition

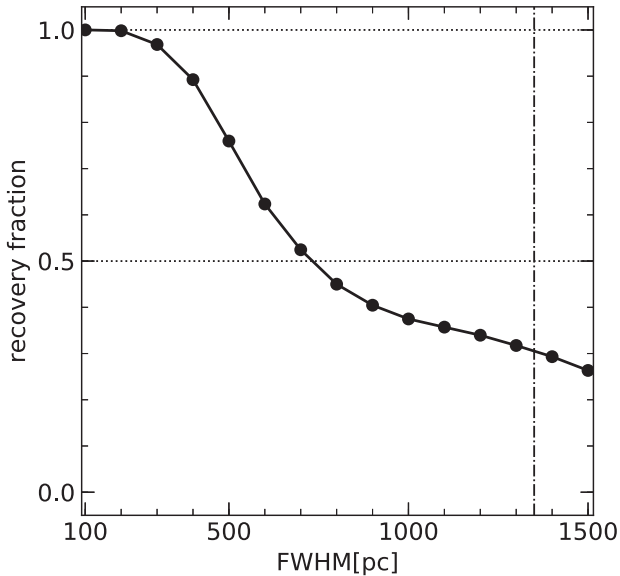


**Figure 6.** Recovery fraction of the Gaussian component as a function of the FWHM. We simulated ALMA observation of the mock Gaussian component with a given FWHM under the same configuration and noise-free condition. The horizontal dashed lines indicate the recovery fraction of 1.0 and 0.5. The vertical dash-dotted line indicates 1350 pc, corresponding to the beam size of Nobeyama 45-m telescope.

by using the task `simobserve` in CASA. After reconstructing the image with `tclean` task, we measured the flux of the component and recovery fraction. Fig. 6 shows the recovery fraction of the Gaussian component as a function of the FWHM. We find that the recovery fraction of the Gaussian component with  $\text{FWHM} \leq 300$  pc is  $\sim 1.0$  and that with  $\text{FWHM} > 300$  pc is under 1.0. For the large Gaussian component with the  $\text{FWHM} \geq 700$  pc, more than half of the flux is missed.

According to the simulation results, total flux of a GMC smaller than  $\sim 300$  pc can be recovered in our observations. Since the radius of the GMCs we identified is smaller than 300 pc (the maximum is  $\sim 100$  pc), their properties would not be affected by the missing flux and the over/underestimates described in Section 5.2.1 would be mainly due to the sensitivity. In our observations, a molecular gas structure larger than  $\sim 700$  pc is mostly resolved out. This result would mainly be responsible for the missing flux in our data and imply the presence of the large-scale gas structures such as diffuse molecular gas components, as have been seen in other galaxies (e.g. M51; Pety et al. 2013). Note that the missing flux would also depend on shape of the GMCs and distribution of them. Thus, it is difficult to figure out the real impact of the missing flux on the GMC properties by simulations. This issue will be expected to be clear by the new ACA observations of NGC 1300 in Cycle 7 (PI: F. Maeda).

## 6 SCALING RELATIONS

In this section, we present the analysis of the scaling relations for the GMCs, which are commonly referred to as Larson’s laws (Larson 1981). Here, we investigate the size–velocity dispersion relation, the virial–luminous mass relation, the size–mass relation, and the relationship between  $\sigma_v^2/R$  and  $\Sigma_{\text{mol}}$  for the resolved GMCs ( $M_{\text{mol}} \geq 5.0 \times 10^5 M_{\odot}$  and  $R > 15$  pc) in NGC 1300. In each analysis, we calculate the Spearman’s rank correlation coefficient ( $r_s$ ) to evaluate the strength of a link between two sets of data. Considering the

number of GMCs, we regard  $r_s \geq 0.8$  as a sign of strong correlation and  $0.5 < r_s < 0.8$  as that of moderate correlation.

### 6.1 Size–velocity dispersion relation

Fig. 7 shows the size–velocity dispersion relation in NGC 1300. The relation in M51 spiral arms from C14 is shown as grey squares. In panel (a), although the majority of the data points lies around the Galactic fit (Solomon et al. 1987), the correlation is not seen ( $r_s = -0.04$ ) which is also observed in M51 spiral arms ( $r_s = 0.16$ ). Even with division into subregions, the correlations are not seen ( $|r_s| < 0.3$ ).

The existence of the size–velocity dispersion relation has been discussed. In M51, there was no correlation in not only spiral arms but also centre and interarm regions (C14). Hirota et al. (2018) reported the apparent lack of correlation in the various environments including arm and bar regions of M83. On the contrary, Bolatto et al. (2008) found a correlation of  $\sigma_v \propto R^{0.60 \pm 0.10}$  for the multigalaxy GMC population including spiral galaxies and dwarf galaxy. Faesi et al. (2018) found also a correlation of  $\sigma_v \propto R^{0.48 \pm 0.05}$  in NGC 300. In Section 6.4, we will discuss the cause for the weak correlation in NGC 1300.

### 6.2 Virial equilibrium

The upper panels in Fig. 8 show the relation between virial mass and the molecular gas mass derived from CO luminosity in NGC 1300. We find moderate correlations for all GMCs ( $r_s = 0.52$ ) in *arm* (0.53) and in *bar-end* (0.70), while there is no apparent correlation in *bar* (0.25). In the panels with  $r_s \geq 0.5$ , a magenta solid line represents the best-fitting line determined by the ordinary least-squares method:  $M_{\text{vir}} \propto M_{\text{mol}}^{0.70 \pm 0.35}$  in the whole region,  $M_{\text{vir}} \propto M_{\text{mol}}^{0.65 \pm 0.55}$  in *arm*, and  $M_{\text{vir}} \propto M_{\text{mol}}^{0.90 \pm 0.53}$  in *bar-end*. These relationships agree with that in M51 spiral arms shown as orange solid line ( $M_{\text{vir}} \propto M_{\text{mol}}^{0.74}$ ). In lower panels of Fig. 8, we plot the virial parameter ( $\alpha_{\text{vir}}$ ) as a function of  $M_{\text{mol}}$ . As inferred from the slope lower than 1.0 in upper panels in Fig. 8,  $\alpha_{\text{vir}} \cong M_{\text{vir}}/M_{\text{mol}}$  decreases with increasing  $M_{\text{mol}}$ . This suggests that the high-mass GMCs tend to be more strongly bound than low-mass GMCs in *arm* and *bar-end* of NGC 1300 as seen in M51.

### 6.3 Size–mass relation

Fig. 9 shows the size–mass relation in NGC 1300. There is a moderate correlation in each panel ( $0.60 < r_s < 0.75$ ). The magenta solid line represents the best-fitting line determined by the ordinary least-squares method. The slope of the relation in *bar* (0.57) is the shallowest, followed by *arm* (1.00) and *bar-end* (1.36). The fact that the index is smaller than 2.0, the molecular gas surface density ( $\Sigma_{\text{mol}}$ ) of GMCs is not roughly constant but decreases with increasing GMC size in NGC 1300. The difference in the index shows that the molecular gas surface density ( $\Sigma_{\text{mol}}$ ) in *bar* is lower than GMCs with similar size in *arm* and *bar-end*, which is consistent with the tendency of  $\Sigma_{\text{mol}}$  (Fig. 5g). The orange solid line represents the best-fitting line for the GMCs ( $M_{\text{mol}} \geq 5.0 \times 10^5 M_{\odot}$  and  $R \geq 15$  pc) in M51 spiral arms and slope is 1.23. The  $\Sigma_{\text{mol}}$  in *bar* and *arm* is lower than GMCs with similar size in M51 spiral arms.

### 6.4 Relationship between $\sigma_v^2/R$ and $\Sigma_{\text{mol}}$

Recent studies on molecular gas at GMC scale argued that the relationship between  $\sigma_v^2/R = c^2$  and  $\Sigma_{\text{mol}}$  is useful to investigate

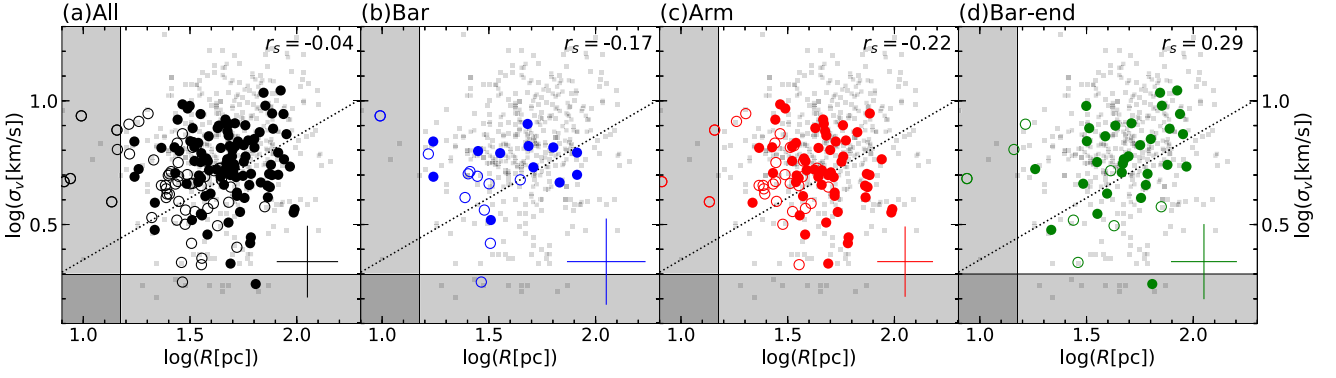


**Figure 7.** (a) Size–velocity dispersion relation for the GMCs in the whole region in NGC 1300. (b)–(d) Same as panel (a) but for the different environments in NGC 1300. We show the GMCs with  $M_{\text{mol}} \geq 5.0 \times 10^5 M_{\odot}$  and  $R \geq 15$  pc in filled circles and the rest in open circles. The average error bars are indicated as a cross in the bottom right corner of each panel. The range below the spatial (15 pc) and spectral ( $2.0 \text{ km s}^{-1}$ ) sensitivity limit is indicated as shaded regions. The Spearman’s correlation rank,  $r_s$ , for the filled circle is given in the top right corner of each panel. The grey squares show the relationship for GMCs in M51 spiral arms (C14). The black dotted line indicates the Galactic fit,  $\sigma_v = 0.72R^{0.5}$  (Solomon et al. 1987).

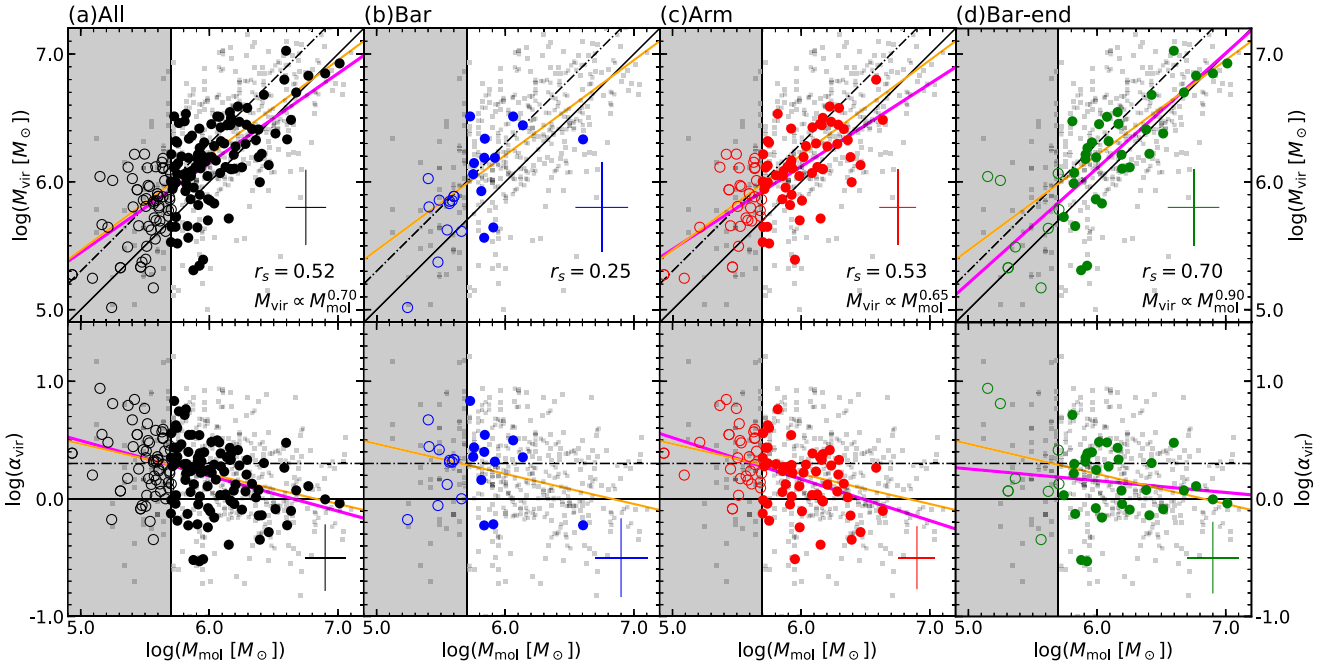


**Figure 8.** (a) Virial mass–luminosity based mass relation (upper) and virial parameter–luminosity based mass relation (lower) for the GMCs in the whole region of NGC 1300. (b)–(d) Same as panel (a) but for the different environments in NGC 1300. We show the GMCs with  $M_{\text{mol}} \geq 5.0 \times 10^5 M_{\odot}$  and  $R \geq 15$  pc in filled circles and the rest in open circles. The average error bars are indicated as a cross in each panel. The range below  $M_{\text{mol}} = 5.0 \times 10^5 M_{\odot}$  is indicated as a shaded region. The black solid and dotted lines indicate the line for  $\alpha_{\text{vir}} = 1.0$  and  $\alpha_{\text{vir}} = 2.0$ , respectively. For upper panels, the Spearman’s correlation rank,  $r_s$ , for the filled circle is given in the bottom right corner (BRC) of each panel. If  $r_s$  is larger than 0.5, we show the best-fitting line as a magenta solid line and its slope is given in the BRC. The grey squares and the orange solid line show the relationship and the best-fitting line for GMCs in M51 spiral arms (C14), respectively.

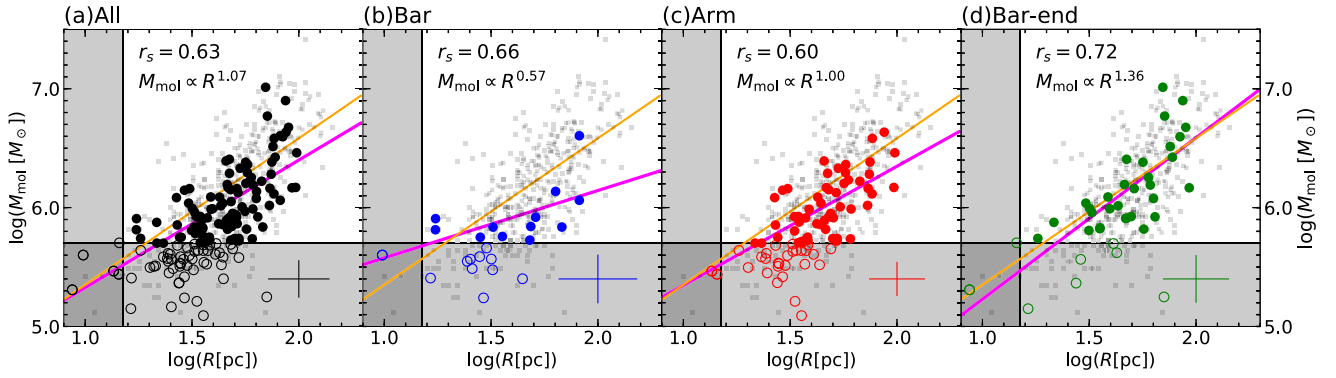
the physical state of the GMCs (e.g. Heyer et al. 2009; Leroy et al. 2015; Sun et al. 2018). This is because the position of the GMC in  $\sigma_v^2/R - \Sigma_{\text{mol}}$  space gives information about not only virial parameter,  $\alpha_{\text{vir}}$ , but also internal turbulent pressure,  $P_{\text{int}}$  of the GMC. Here, the  $P_{\text{int}}$  can be expressed as

$$\begin{aligned} \frac{P_{\text{int}}}{k} &= \frac{\rho \sigma_v^2}{k} \\ &= 3695 \left( \frac{\Sigma_{\text{mol}}}{M_{\odot} \text{ pc}^{-2}} \right) \left( \frac{c}{\text{km s}^{-1} \text{ pc}^{-0.5}} \right)^2 \text{ [cm}^{-3} \text{ K]}, \end{aligned} \quad (7)$$

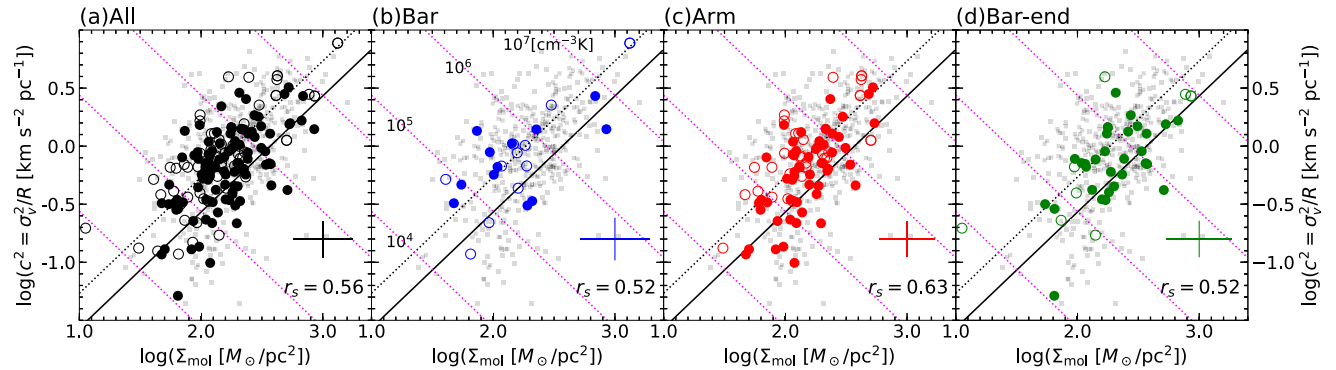
where  $\rho$  is the molecular gas volume density of the GMC.

Fig. 10 plots the  $\sigma_v^2/R - \Sigma_{\text{mol}}$  relation of NGC 1300. The  $\alpha_{\text{vir}} = 1$  and 2 are represented by a black solid and a dotted line, respectively, and the magenta dotted lines indicate constant  $P_{\text{int}}$ . Note that the  $\sigma_v^2/R - \Sigma_{\text{mol}}$  relation is mathematically equivalent to the  $M_{\text{vir}} - M_{\text{mol}}$  relation (Fig. 8). We can see a moderate correlation in the whole region ( $r_s = 0.63$ ), bar (0.66), arm (0.60), and bar-end (0.72) in NGC 1300, which shows the scaling coefficient,  $c$ , increases with increasing  $\Sigma_{\text{mol}}$ . The same tendency is seen in Milky Way; Heyer et al. (2009) pointed out that  $c$  is proportional to  $\Sigma_{\text{mol}}^{1/2}$ .

As shown in panel (a),  $P_{\text{int}}$  of the GMCs in NGC 1300 is spread about 3 dex ( $10^4 \leq P_{\text{int}}/k/\text{[cm}^{-3} \text{ K]} \leq 10^7$ ). The median values



**Figure 9.** (a) Size–molecular gas mass relation for the GMCs in the whole region of NGC 1300. (b)–(d) Same as panel (a) but for the different environments in NGC 1300. We show the GMCs with  $M_{\text{mol}} \geq 5.0 \times 10^5 M_{\odot}$  and  $R \geq 15$  pc in filled circles and the rest in open circles. The average error bars are indicated as a cross in each panel. The range below  $M_{\text{mol}} = 5.0 \times 10^5 M_{\odot}$  and  $R = 15$  pc is indicated as shaded regions. The Spearman’s correlation rank,  $r_s$ , for the filled circle is given in the top left corner (TLC) of each panel. We show the best-fitting line as a magenta solid line and its slope is given in the TLC. The grey squares and the orange solid line show the relationship and the best-fitting line for GMCs in M51 spiral arms (C14), respectively.



**Figure 10.** (a) Scale coefficient as a function of molecular gas surface density in the whole region of NGC 1300. (b)–(d) Same as panel (a) but for the different environments in NGC 1300. We show the GMCs with  $M_{\text{mol}} \geq 5.0 \times 10^5 M_{\odot}$  and  $R \geq 15$  pc in filled circles and the rest in open circles. The average error bars are indicated as a cross in each panel. The Spearman’s correlation rank,  $r_s$ , for the filled circle is given in the BRC of each panel. The grey squares show the relationship for the GMCs in M51 spiral arms (C14). The black solid line and the dotted line indicate the lines for  $\alpha_{\text{vir}} = 1.0$  and  $2.0$ , respectively. The magenta dotted lines indicate the line for  $P_{\text{int}}/k = 10^4, 10^5, 10^6,$  and  $10^7$  [cm $^{-3}$  K].

and the  $\Delta Q$  of  $P_{\text{int}}/k$  are roughly constant across the different environments:  $2.2^{+6.2}_{-1.4}$ ,  $2.9^{+4.6}_{-2.5}$ , and  $3.3^{+10.5}_{-1.6} \times 10^5$  cm $^{-3}$  K in *bar*, *arm*, and *bar-end*, respectively. The K-S tests give high  $p$ -values of  $>0.1$ . These values are slightly lower than that in M51 spiral arms of  $6.7^{+8.3}_{-4.3} \times 10^5$  cm $^{-3}$  K.

Fig. 10 can be interpreted to explain the cause for weak correlation between size and velocity dispersion (Fig. 7). The GMCs in NGC 1300 cover a wider range of  $\Sigma_{\text{mol}}$  ( $\sim 1.5$  dex) than those in Milky Way ( $\sim 1.0$  dex; Solomon et al. 1987). Therefore, the range of  $c$  in NGC 1300 becomes wider than that in Milky Way, leading to a decorrelation between  $\sigma_v$  and  $R$ . The dependence of the  $c$  on the  $\Sigma_{\text{mol}}$  also may be the part of the cause of weak correlation seen in M51 and M83 (see Hirota et al. 2018). Note that the limited dynamic range of the size parameter and the errors in the measurements with CPROPS could be responsible for the weak correlation.

## 7 GMC MASS SPECTRA

In this section, we investigate the mass spectra of GMCs in NGC 1300. The mass spectrum provides information about GMCs formation and destruction processes (e.g. Kobayashi et al. 2017), and is usually expressed in differential form known to follow a

power-law relation as

$$\frac{dN}{dM} \propto M^{\gamma}, \quad (8)$$

where  $M$  is the molecular gas mass,  $N$  is the number of molecular clouds, and  $\gamma$  is an index of the power-law relation.

Integration of this expression gives a cumulative mass distribution. Several studies reported the GMC mass spectra are underpopulated at higher masses, i.e. it is thought that there is an upper limit to the GMC mass (e.g. Williams & McKee 1997; Fukui et al. 2001, 2008; Rosolowsky 2007; Gratier et al. 2012). Considering the existence of the upper cut-off mass, a truncated power law is suitable as a cumulative mass spectrum (Williams & McKee 1997):

$$N(> M) = -\frac{N_u}{\gamma + 1} \left[ \left( \frac{M}{M_u} \right)^{\gamma+1} - 1 \right], \quad (9)$$

where  $M_u$  is an upper cut-off mass of GMCs and  $N_u$  is a measure of the number of GMCs at the upper cut-off mass. The index  $\gamma$  shows how the GMC mass is distributed. If  $\gamma$  is larger than  $-2$ , massive GMCs dominate the total cloud mass.

The parameters of the mass spectrum ( $\gamma$  and  $M_u$ ) is considered to be determined in the balance between the formation and destructive

processes of GMCs. Enhancement of the formation process of massive GMCs (e.g. agglomeration of small clouds and self-gravity; Dobbs 2008) leads to a steeper mass spectrum and a higher  $M_u$ . On the contrary, the destruction process [e.g. stellar feedback, cloud–cloud collision (CCC), and large-scale shear motion] plays a role to make mass spectrum shallow and decrease the  $M_u$ .

Fig. 11 shows the cumulative GMC mass spectrum in different environments in NGC 1300 (panel a–d) and in M51 spiral arms (panel e; C14). The y-axis shows the GMC number density. The number density of high-mass GMC ( $M_{\text{mol}} \geq 1.0 \times 10^6 M_\odot$ ) in *bar-end* is the highest ( $5.2 \text{ kpc}^{-2}$ ), followed by that in *bar* ( $1.2 \text{ kpc}^{-2}$ ) and *arm* ( $2.6 \text{ kpc}^{-2}$ ). Although these values depend on the definition of the environmental mask, there is no doubt that the number densities of high-mass GMC with  $\geq 1.0 \times 10^6 M_\odot$  in *bar* ( $5.1 \text{ kpc}^{-2}$ ) and *arm* ( $9.9 \text{ kpc}^{-2}$ ) are lower than that in *bar-end* ( $3.6 \text{ kpc}^{-2}$ ). In particular, GMCs more than  $5.0 \times 10^6 M_\odot$  are only observed in *bar-end*. Note that the number density in M51 spiral arms is  $18.2 \text{ kpc}^{-2}$ , and is the factor of 4–10 larger than that in any environments of NGC 1300.

We fitted the cumulative GMC mass spectrum with equation (9). Although the mass completeness limit is expected to be  $2.0 \times 10^5 M_\odot$  in uncrowded regions (see Section 5), the completeness limit might be effectively raising in a crowded region like *bar-end* (e.g. Colombo et al. 2014; Hirota et al. 2018). Thus, we fitted the mass spectrum using the GMCs with  $M_\odot \geq 5.0 \times 10^5 M_\odot$  indicated as a vertical black dash–dotted line in Fig. 11. To estimate the fitting uncertainties, we made resampling with 100 realizations. In one realization, random values of a molecular gas mass were generated within the uncertainties CPROPS calculated. The median and the MAD of 100 realizations for each parameter were adopted as the best-fitting value and the confidence interval (Table 5). The orange solid line in Fig. 11 shows the best-fitting cumulative mass function. We list the  $p$ -values of the K-S tests as an indication of the goodness of fit in the last column of Table 5. Here, we fitted the mass spectrum of GMCs in M51 spiral arms in the same way.

No clear difference was found in the shape of mass spectra between *bar* and *arm*: the slope and upper mass limit is  $\gamma \sim -2.0$  and  $M_u \sim 5.0 \times 10^6 M_\odot$ , respectively. However, the mass spectrum in *bar-end* is obviously different from those in *bar* and *arm*. The slope in *bar-end* is flatter than  $-2$ , which indicates that massive GMCs account for a large population of total cloud mass in *bar-end*. The upper mass limit in *bar-end* of  $M_u = (1.3 \pm 3.4) \times 10^7 M_\odot$  is twice as large as that in *bar* and *arm* regions. The presence or absence of differences in the mass spectrum between environments is consistent with that in the box plot of  $M_{\text{mol}}$  (see Section 5.1). The  $\gamma$  and  $M_u$  in *bar-end* are similar to those in M51 spiral arms.

Since the  $\gamma$  in *bar-end* is larger than those in *bar* and *arm*, *bar-end* would be an environment where the massive GMCs form more than in *bar* and *arm*. The similarity of the feature between *bar-end* and M51 spiral arms suggests the mechanism which regulate the formation and destruction of GMCs is similar to that in M51 spiral arms. Although the mass spectra in *bar* and *arm* is similar, the GMC destruction mechanism would be different because the star formation activity is apparently different (Section 1). The stellar feedback process may be predominant in *arm*, but the dynamical effect (e.g. CCC and large-scale shear motion) may be an important process in *bar*.

## 8 DISCUSSION

As described in Sections 1 and 3, SFE differences with environments are clearly seen in typical strongly barred galaxies. In the arms, H II regions are associated with dust lanes, and GMCs coexist with

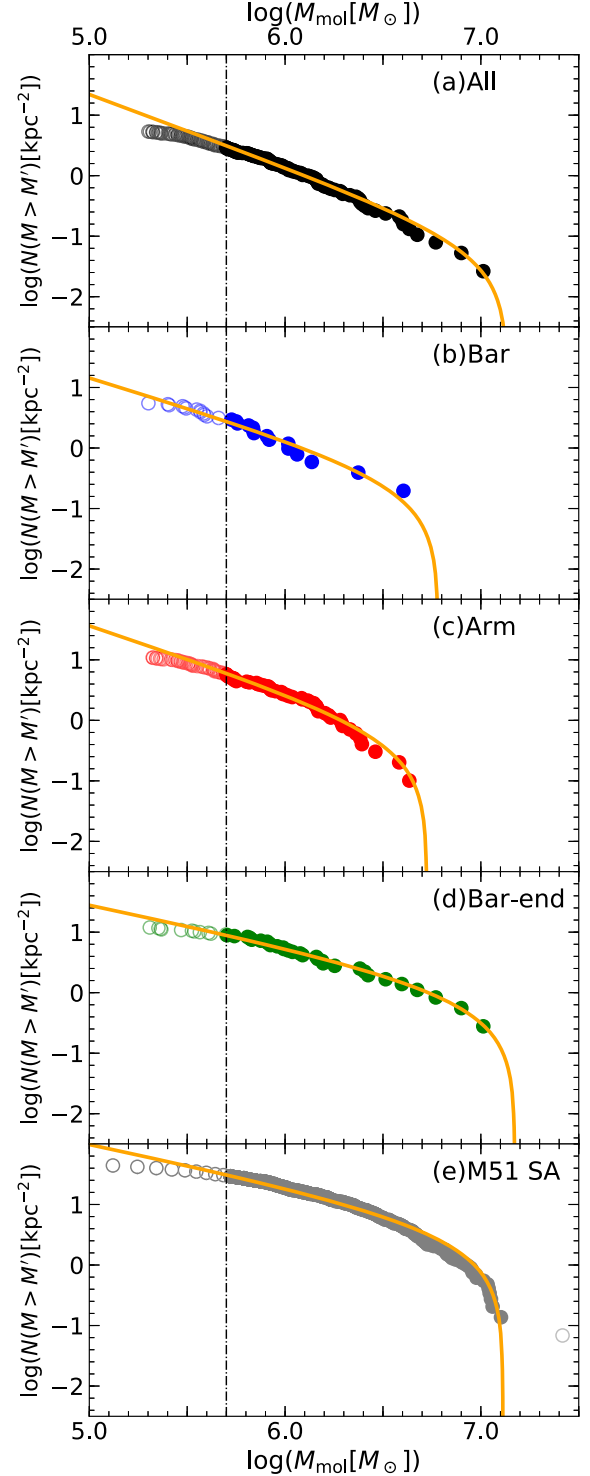


**Figure 11.** (a) Cumulative mass spectrum for GMCs in the whole region of NGC 1300. (b)–(d) Same as panel (a), but for the different environments in NGC 1300. (e) Same as panel (a), but for GMCs in M51 spiral arms (C14). In each plot, the filled and open circles indicate the GMCs that are and are not used for fitting the spectrum with equation (9), respectively. The orange solid line indicates the best-fitting function. The dash–dotted vertical line indicates the lower mass limit,  $5 \times 10^5 M_\odot$ , for the fitting of mass spectra.

**Table 5.** Truncated power-law fits to the GMC mass spectra in different environments in NGC 1300.

Envir.	$\gamma$	$M_u$ ( $10^6 M_\odot$ )	$N_u$	$p$ -value
All	$-2.20 \pm 0.04$	$13.6 \pm 0.67$	$2.74 \pm 0.40$	0.22
Bar	$-1.97 \pm 0.20$	$6.26 \pm 3.04$	$1.36 \pm 0.97$	0.59
Arm	$-2.08 \pm 0.10$	$5.31 \pm 0.36$	$5.45 \pm 1.07$	0.40
Bar-end	$-1.66 \pm 0.07$	$14.8 \pm 0.93$	$2.56 \pm 0.42$	0.85
M51 SA	$-1.70 \pm 0.03$	$13.0 \pm 0.34$	$35.6 \pm 2.46$	$10^{-4}$

*Note.* Slopes  $\gamma$ , upper cut-off mass  $M_u$ , and a measure of the number of GMCs at the upper cut-off mass  $N_u$  of the truncated power-law fits to the GMC mass spectra of the different environments in NGC 1300. The errors are obtained through 100 resampling interaction. In the last column, we list the  $p$ -values of the K-S tests as an indication of the goodness of fit.

the dust lanes. However, in bar regions, prominent HII regions are often not seen while the GMCs do exist. What physical mechanism controls the SFE of the GMC? Based on the K-S tests, there is no significant variation in the physical properties ( $\sigma_v$ ,  $R$ ,  $M_{\text{mol}}$ ,  $M_{\text{vir}}$ ,  $\Sigma_{\text{mol}}$ ,  $\alpha_{\text{vir}}$ , and  $c$ ) of the GMCs between *bar* and *arm* (Table 4). Comparing to the GMCs between *bar* and *bar-end*, and *arm* and *bar-end*, (marginally) significant difference is only seen in the distribution of  $M_{\text{mol}}$ . Therefore, it appears that systematic differences in the GMC properties are not the cause for the SFE differences with environments.

Many previous studies investigated the cause for the low SFE in the bar regions. Some previous studies proposed that GMCs cannot form due to a strong shock and/or shear along the bar (e.g. Tubbs 1982; Athanassoula 1992; Reynaud & Downes 1998). Recent studies suggest molecular clouds in bar regions may be gravitationally unbound due to the strong internal turbulence of the clouds. Sorai et al. (2012) made  $^{12}\text{CO}(1-0)$  map of Maffei 2 at an angular resolution of 200 pc, and pointed out a possibility that clouds in the bar regions are gravitationally unbound, which causes the low SF activity. Nimori et al. (2013) performed a two-dimensional hydrodynamical simulation and also found the unbound clouds in bars. In NGC 1300, the number fraction of GMC with  $\alpha_{\text{vir}} > 2$  in *bar* (60 per cent) is larger than that in *arm* and *bar-end* (30 per cent), which may partly contribute to decreasing the SFE in the bar region. However, there is no significant difference in  $\alpha_{\text{vir}}$  based on the K-S test (Table 4). This result suggests that the lack of massive star formation in the strong bar of NGC 1300 cannot be explained by a systematic difference of  $\alpha_{\text{vir}}$  only.

Hirota et al. (2018) found the  $\alpha_{\text{vir}}$  of the GMCs in the bar of M83 (median is  $\sim 1.6$ ) is larger than that in the arm ( $\sim 1.2$ ). This result seems to be inconsistent with our results. However, a direct comparison with our results is not straightforward because the algorithm for identifying GMCs they used was different from ours. It is necessary to compare the GMC properties between M83 and NGC 1300 under the same data quality and methodology. This comparison is important but beyond our scope in this paper, which remains as a future subject.

Although the galactic environments seem not to affect the physical properties of GMCs in NGC 1300, there is a possibility that the interaction of GMCs is affected. CCCs, which induce clump formation by shock compressions, have been suggested as the mechanism of massive star formation (e.g. Habe & Ohta 1992; Fukui et al. 2014). Recent studies suggest that the efficiency of massive star formation strongly depends on the collision speed. Takahira, Tasker & Habe (2014) and Takahira et al. (2018) per-

formed hydrodynamical simulations of CCCs. They found that massive clumps ( $\sim 100M_\odot$ ) finally form in the case of slower CCCs ( $\sim 5 \text{ km s}^{-1}$ ). However, in faster CCCs ( $> 10 \text{ km s}^{-1}$ ), clouds are highly compressed, but the duration of the collision is not long enough for the clump mass to grow via gas accretion and no massive clump is formed. Based on high-resolution ( $\sim$  a few pc) 3D hydrodynamical simulations aiming at modelling a barred galaxy M83, Fujimoto, Tasker & Habe (2014) found that collision speed among clouds in bar regions is faster than in arm regions and proposed this difference makes SFE variations.

CO observations towards NGC 1300 with a single-dish telescope of Nobeyama 45-m show the higher velocity dispersion in bar regions than in arm regions at a kpc-scale resolution (Maeda et al. 2018). This result suggests the relative velocity among the clouds in the bar regions is larger than that in the arm regions and is qualitatively consistent with the fast CCC scenario in the bar region. Other CO observations towards barred galaxies with a single-dish telescope show the same tendency (e.g. Regan, Sheth & Vogel 1999; Morokuma-Matsui et al. 2015; Muraoka et al. 2016; Yajima et al. 2019). Egusa et al. (2018) find that a probability distribution function of velocity dispersion in the bar of M83 is systematically larger than in the arm (see also Sun et al. 2018). Querejeta et al. (2019) found a significant anticorrelation between the SFE and velocity dispersion of the dense gas at a 100 pc scale in M51. The velocity dispersion of the dense gas is thought to be largely reflecting velocity dispersion among different clumps. According to these results, the difference in SFE between the arm and bar regions would be due to the difference in CCC speed rather than the difference in the physical properties of the GMCs.

Fujimoto et al. (submitted) present a hydrodynamical simulation of a strongly barred galaxy, using a stellar potential model of NGC 1300. They found that there is no significant environmental dependence of cloud properties including the virial parameter, which is consistent with our result presented in this paper. Further, they show that the collision speed in the bar is significantly faster than the other regions due to the elongated global gas motion by the stellar bar. The fraction of colliding clouds with collision speed more than  $20 \text{ km s}^{-1}$  in bar regions ( $\sim 40$  per cent) is significantly larger than those in other regions ( $< 10$  per cent). They conclude that the physical mechanism that causes the lack of active star-forming regions in the bar of strongly barred galaxies is the high-speed CCCs.

The CCC occurs only a few times within 1 Myr in the bar and arm regions and the effects of collision do not last for long time; the excited internal gas motion induced by the collision decays quickly within at most a few Myr, which is thought to be shorter than cloud lifetimes (10–40 Myr; e.g. Kawamura et al. 2009; Meidt et al. 2015; Chevance et al. 2019; Fujimoto et al. 2019). Therefore, in a snapshot of the galaxy, there are a few or less GMCs affected by the collision in the bar and arm regions. Thus, the GMC properties observed would not be affected by this effect.

As a next step of this study, we should directly compare the simulation of Fujimoto et al. (submitted) and our observational data to investigate the relative velocity among GMCs we detected. Although direct measurement of collision speed from observation data is difficult, the velocity deviation between the GMCs and their surrounding GMCs can be an observable indicator of the collision speed of clouds. Fujimoto et al. (submitted) found that the velocity deviation in the bar region is larger than that in the arm region, which reflects the fast CCCs in the bar. Whether the same tendency is seen in NGC 1300 or not will be clarified by further investigations using our GMC catalogue (Maeda et al., in prep).

## 9 SUMMARY

We made  $^{12}\text{CO}(1-0)$  observations towards the strongly barred galaxy NGC 1300 at a high angular resolution about 40 pc with ALMA. We detected CO emissions from the western arm to the bar region. Using the CPROPS algorithm, we identified 233 GMCs (34, 119, and 49 in *bar*, *arm*, and *bar-end*, respectively) with  $S/N > 4$ . We measured  $R$ ,  $\sigma_v$ , and  $L_{\text{CO}}$  of these GMCs and then derived  $M_{\text{mol}}$ ,  $M_{\text{vir}}$ ,  $\Sigma_{\text{mol}}$ ,  $\alpha_{\text{vir}}$ , and  $c$  of them. We focus on a mass completed sample with  $M_{\text{mol}} > 2.0 \times 10^5 M_{\odot}$  for the investigation of  $T_{\text{peak}}$ ,  $\sigma_v$ , and  $M_{\text{mol}}$  and a resolved sample with  $M_{\text{mol}} > 5.0 \times 10^5 M_{\odot}$  and  $R > 15$  pc for the investigation of  $R$ ,  $M_{\text{vir}}$ ,  $\Sigma_{\text{mol}}$ ,  $\alpha_{\text{vir}}$ , and  $c$ . We compare the GMC properties among the environments. The main results are as follows:

(i) Based on the two-sided K-S tests, there is a significant environmental variation in the  $T_{\text{peak}}$ ; the highest value in *bar-end* followed by *arm* and *bar*. However, there is hardly any significant variations in GMC physical properties ( $\sigma_v$ ,  $R$ ,  $M_{\text{mol}}$ ,  $M_{\text{vir}}$ ,  $\Sigma_{\text{mol}}$ ,  $\alpha_{\text{vir}}$ , and  $c$ ; Fig. 5); (marginally) significant difference is only seen in the distribution of  $M_{\text{mol}}$  between *bar* and *bar-end*, and *arm* and *bar-end* (Table 4). The properties of GMCs in NGC 1300 are roughly comparable to those in M51 spiral arms. In particular, the properties in *bar-end* are very similar.

(ii) We find no obvious  $R$ - $\sigma_v$  relation although the majority of the data points lies around the Galactic fit (Fig. 7). For the relation between  $M_{\text{vir}}$  and  $M_{\text{mol}}$ , there is a moderate correlation in *arm* and *bar-end*, while there is no apparent correlation in *bar* (Fig. 8). We find the  $\alpha_{\text{vir}}$  decreases with increasing  $M_{\text{mol}}$ , which suggests the high-mass GMCs tend to be strongly bound as seen in M51. There is a moderate correlation between  $R$  and  $M_{\text{mol}}$  in each environment (Fig. 9). Further, we find the  $P_{\text{int}}/k$  is roughly constant across the different environments in NGC 1300 (Fig. 10).

(iii) No clear difference is found in the shape of GMC mass spectra between *bar* and *arm*. The slope of the spectrum in the *bar-end* is slightly flatter than those in *arm* and *bar*, and massive GMCs are seen only in the *bar-end* (Fig. 11). The similarity of the feature between *bar-end* and M51 spiral arms suggests the mechanism regulating formation and destruction of GMCs is similar to that in M51 spiral arms.

(iv) It appears that systematic differences in the physical properties of the GMCs are not the cause for the low SFE in the bar region. Other mechanisms such as fast CCCs may control the SFE of GMCs in NGC 1300 (Section 8).

## ACKNOWLEDGEMENTS

We would like to thank the referee for useful comments and suggestions. We are grateful to K. Nakanishi, F. Egusa, Y. Miyamoto, K. Saigo, R. Kawabe, and the staff at the ALMA Regional Center for their help in data reduction. FM is supported by Research Fellowship for Young Scientists from the Japan Society of the Promotion of Science (JSPS). KO is supported by Grants-in-Aids for Scientific Research (C) (16K05294 and 19K03928) from JSPS. AH is funded by the JSPS KAKENHI Grant Number JP19K03923. This paper makes use of the following ALMA data: ADS/JAO.ALMA#2017.1.00248.S. ALMA is a partnership of ESO (representing its member states), NSF (USA) and NINS (Japan), together with NRC (Canada), MOST and ASIAA (Taiwan), and KASI (Republic of Korea), in cooperation with the Republic of Chile. The Joint ALMA Observatory is operated by ESO, AUI/NRAO, and NAOJ. Data analysis was in part carried out on the Multi-

wavelength Data Analysis System operated by the Astronomy Data Center (ADC), National Astronomical Observatory of Japan.

## REFERENCES

- Athanassoula E., 1992, *MNRAS*, 259, 345  
 Bertoldi F., McKee C. F., 1992, *ApJ*, 395, 140  
 Bigiel F., Leroy A., Walter F., Brinks E., de Blok W. J. G., Madore B., Thornley M. D., 2008, *AJ*, 136, 2846  
 Bolatto A. D., Leroy A. K., Rosolowsky E., Walter F., Blitz L., 2008, *ApJ*, 686, 948  
 Chevance M. et al., 2019, *MNRAS*, 493, 2872  
 Colombo D. et al., 2014, *ApJ*, 784, 3  
 Cornwell T. J., 2008, *IEEE J. Sel. Top. Signal Process.*, 2, 793  
 Dobbs C. L., 2008, *MNRAS*, 391, 844  
 Egusa F., Hirota A., Baba J., Muraoka K., 2018, *ApJ*, 854, 90  
 England M. N., 1989, *ApJ*, 337, 191  
 Faesi C. M., Lada C. J., Forbrich J., 2018, *ApJ*, 857, 19  
 Fujimoto Y., Tasker E. J., Habe A., 2014, *MNRAS*, 445, L65  
 Fujimoto Y., Chevance M., Haydon D. T., Krumholz M. R., Kruijssen J. M. D., 2019, *MNRAS*, 487, 1717  
 Fukui Y., Mizuno N., Yamaguchi R., Mizuno A., Onishi T., 2001, *PASJ*, 53, L41  
 Fukui Y. et al., 2008, *ApJS*, 178, 56  
 Fukui Y. et al., 2014, *ApJ*, 780, 36  
 Gallagher M. J. et al., 2018, *ApJ*, 858, 90  
 Gratier P. et al., 2012, *A&A*, 542, A108  
 Habe A., Ohta K., 1992, *PASJ*, 44, 203  
 Heyer M., Krawczyk C., Duval J., Jackson J. M., 2009, *ApJ*, 699, 1092  
 Hirota A. et al., 2014, *PASJ*, 66, 46  
 Hirota A. et al., 2018, *PASJ*, 70, 73  
 Hughes A. et al., 2013, *ApJ*, 779, 46  
 Kawamura A. et al., 2009, *ApJS*, 184, 1  
 Kennicutt Robert C. J., 1998, *ARA&A*, 36, 189  
 Kobayashi M. I. N., Inutsuka S.-i., Kobayashi H., Hasegawa K., 2017, *ApJ*, 836, 175  
 Larson R. B., 1981, *MNRAS*, 194, 809  
 Leroy A. K. et al., 2013, *AJ*, 146, 19  
 Leroy A. K. et al., 2015, *ApJ*, 801, 25  
 Longmore S. N. et al., 2013, *MNRAS*, 429, 987  
 Maeda F., Ohta K., Fujimoto Y., Habe A., Baba J., 2018, *PASJ*, 70, 37  
 Meidt S. E. et al., 2015, *ApJ*, 806, 72  
 Momose R., Okumura S. K., Koda J., Sawada T., 2010, *ApJ*, 721, 383  
 Morokuma-Matsui K., Sorai K., Watanabe Y., Kuno N., 2015, *PASJ*, 67, 2  
 Mould J. R. et al., 2000, *ApJ*, 529, 786  
 Muraoka K. et al., 2016, *PASJ*, 68, 89  
 Nimori M., Habe A., Sorai K., Watanabe Y., Hirota A., Namekata D., 2013, *MNRAS*, 429, 2175  
 Pan H.-A., Kuno N., 2017, *ApJ*, 839, 133  
 Pety J. et al., 2013, *ApJ*, 779, 43  
 Querejeta M. et al., 2019, *A&A*, 625, A19  
 Regan M. W., Sheth K., Vogel S. N., 1999, *ApJ*, 526, 97  
 Reynaud D., Downes D., 1998, *A&A*, 337, 671  
 Rich J. W., de Blok W. J. G., Cornwell T. J., Brinks E., Walter F., Bagetakos I., Kennicutt R. C. J., 2008, *AJ*, 136, 2897  
 Rosolowsky E., 2007, *ApJ*, 654, 240  
 Rosolowsky E., Leroy A., 2006, *PASP*, 118, 590  
 Sandage A., Tammann G. A., 1981, *A Revised Shapley-Ames Catalog of Bright Galaxies*. Carnegie Institution, Washington  
 Schinnerer E. et al., 2013, *ApJ*, 779, 42  
 Schrub A. et al., 2011, *AJ*, 142, 37  
 Solomon P. M., Rivolo A. R., Barrett J., Yahil A., 1987, *ApJ*, 319, 730  
 Sorai K. et al., 2012, *PASJ*, 64, 51  
 Stephens M. A., 1970, *J. R. Stat. Soc. B*, 32, 115  
 Sun J. et al., 2018, *ApJ*, 860, 172  
 Takahira K., Tasker E. J., Habe A., 2014, *ApJ*, 792, 63  
 Takahira K., Shima K., Habe A., Tasker E. J., 2018, *PASJ*, 70, S58

Tubbs A. D., 1982, *ApJ*, 255, 458  
 Usero A. et al., 2015, *AJ*, 150, 115  
 Watanabe Y., Sorai K., Kuno N., Habe A., 2011, *MNRAS*, 411, 1409  
 Williams J. P., McKee C. F., 1997, *ApJ*, 476, 166  
 Yajima Y. et al., 2019, *PASJ*, 71, S13

## SUPPORTING INFORMATION

Supplementary data are available at [MNRAS](https://www.mnras.org/online) online.

### Table B1. GMC catalogue.

Please note: Oxford University Press is not responsible for the content or functionality of any supporting materials supplied by the authors. Any queries (other than missing material) should be directed to the corresponding author for the article.

## APPENDIX A: CPROPS BIAS

CPROPS corrects for the sensitivity by extrapolating GMC properties to those we would expect to measure with perfect sensitivity (i.e. 0 K). As described in Section 4.2.1, the extrapolated  $R$ ,  $\sigma_v$ , and  $L_{\text{CO}}$  is typically 1.5–2.0 times higher than the directly measured values. CPROPS also corrects for the resolution by deconvolution for beam and channel width. The corrected  $R$ ,  $\sigma_v$  is typically by a factor of 0.7–0.8 lower than the extrapolated values. Since the

accuracy of these corrections (extrapolation and deconvolution) depends on the sensitivity, spatial resolution and velocity resolution (Rosolowsky & Leroy 2006), it is necessary to assess the reliability of the measurements of GMC properties.

Using CASA, we simulated ALMA observation of mock GMCs, which are three-dimensional Gaussian clouds with a given  $M_{\text{mol}}$ ,  $R$ , and  $\sigma_v$  in a position–position–velocity space. We create a fits image with 100 mock GMCs centred in fixed positions. The  $M_{\text{mol}}$ ,  $R$ , and  $\sigma_v$  are randomly determined in the range of  $5.3 \leq \log(M_{\text{mol}}/[M_{\odot}]) \leq 6.8$ ,  $1.5 \leq \log(R[\text{pc}]) \leq 2.2$ , and  $0.3 \leq \log(\sigma_v/[\text{km s}^{-1}]) \leq 1.1$ , respectively. The GMCs are round clouds (i.e. axial ratio = 1.0). Here, we assume the CO-to-H<sub>2</sub> conversion factor of  $4.4 M_{\odot} (\text{K km s}^{-1} \text{pc}^2)^{-1}$ . Then, using the task of `simobserve` in CASA, we simulate observation under the same configuration, pointings, and noise condition of our ALMA observations (see Section 2). After reconstructing the image with the same `clean` parameters (see Section 2), we identify the GMCs using CPROPS with the same settings described in Section 4. We repeated this procedure 12 times, and then we extracted the GMCs with  $4 \leq \text{S/N} \leq 10$ , corresponding to the observed value.

Fig. A1 shows the results of this simulation. The superscript *in* denotes the input value of the mock GMC and *out* denotes the output value CPROPS measured and corrected. We plot the ratio of output value to input value as a function of input value for  $\sigma_v$ ,  $R$ , and  $M_{\text{mol}}$ , dividing GMCs into lower S/N ( $4 \leq \text{S/N} < 7$ ) and higher S/N ( $7 \leq$

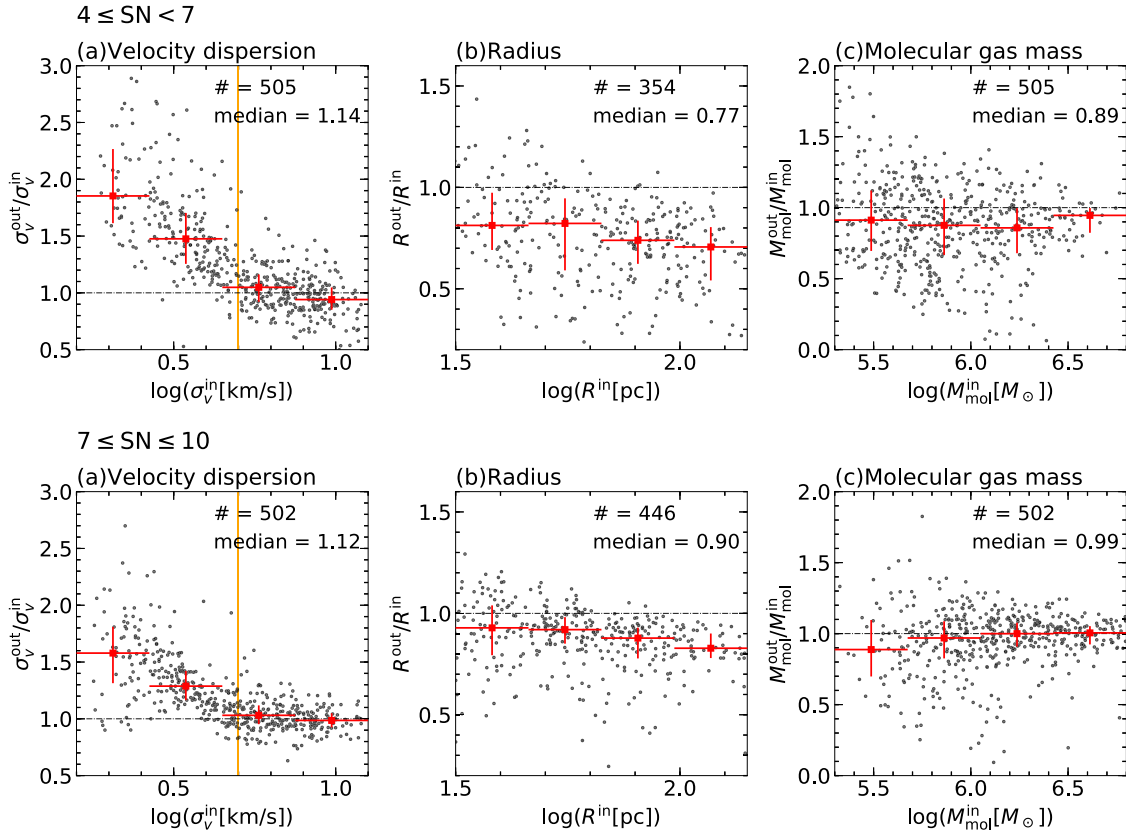


**Figure A1.** Results of the ALMA observation simulation of the mock GMCs. (a): Ratio of the output velocity dispersion by CPROPS ( $\sigma_v^{\text{out}}$ ) to the input (model) velocity dispersion ( $\sigma_v^{\text{in}}$ ) as a function of the  $\sigma_v^{\text{in}}$ . We show the GMCs with lower S/N ( $4 \leq \text{S/N} < 7$ ) and higher S/N ( $7 \leq \text{S/N} \leq 10$ ) in upper and lower panel, respectively. The red square shows the median value in a bin whose range is shown as error bar in x-axis, and an error bar in y-axis shows the  $\Delta Q$  in the bin. The orange solid line shows the channel width of 5.0 km s<sup>-1</sup>. The black dash-dotted line shows  $\sigma_v^{\text{out}}/\sigma_v^{\text{in}} = 1.0$ . (b),(c): Same as panel (a) but for radius and molecular gas mass.

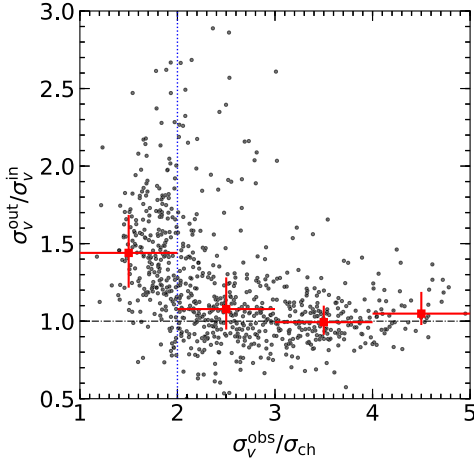


**Figure A2.** Ratio of the output velocity dispersion by CPROPS ( $\sigma_v^{\text{out}}$ ) to the input (model) velocity dispersion ( $\sigma_v^{\text{in}}$ ) as a function of the velocity dispersion without CPROPS correction ( $\sigma_v^{\text{obs}}$ ) to channel width ( $\sigma_{\text{ch}} = \sqrt{\Delta V_{\text{chan}}^2/2\pi} = 2.0 \text{ km s}^{-1}$ ). The red square shows the median value in a bin whose range is shown as error bar in x-axis, and a error bar in y-axis shows the  $\Delta Q$  in the bin. The black dash-dotted line shows  $\sigma_v^{\text{out}}/\sigma_v^{\text{in}} = 1.0$ . The blue dotted line shows  $\sigma_v^{\text{obs}}/\sigma_{\text{ch}} = 2.0$ .

$S/N \leq 10$ ). In panel (a), we find CPROPS measurements work well for the GMCs whose  $\sigma_v^{\text{in}}$  is larger than  $5.0 \text{ km s}^{-1}$ . However, for the GMCs with  $\sigma_v^{\text{in}} \leq 5.0 \text{ km s}^{-1}$ , CPROPS overestimates  $\sigma_v$  by a factor of  $\sim 1.5$  regardless of  $S/N$ .

According to Rosolowsky & Leroy (2006), the extrapolation works well regardless of the  $S/N$ , if the line width of the identified GMC is at least twice the channel width. In Fig. A2, we plot the  $\sigma_v^{\text{out}}/\sigma_v^{\text{in}}$  as a function of the ratio of the velocity dispersion without CPROPS correction ( $\sigma_v^{\text{obs}}$ ) to channel width ( $\sigma_{\text{ch}} = \sqrt{\Delta V_{\text{chan}}^2/2\pi} = 2.0 \text{ km s}^{-1}$ ). We find that the  $\sigma_v^{\text{out}}$  is overestimated by a factor of  $\sim 1.5$  if the  $\sigma_v^{\text{obs}}$  is less than half the channel width. Such GMC accounts for 56 per cent, 64 per cent, and 64 per cent in *bar*, *arm*, and *bar-end*, respectively. Therefore, a large number of the catalogued GMCs may be overestimated in the  $\sigma_v$  by a factor of  $\sim 1.5$ .

The CPROPS algorithm performs relatively well for the measurements of the  $M_{\text{mol}}$  and  $R$  in comparison to  $\sigma_v$ . In panel (b), we find CPROPS slightly underestimate radius: the  $R^{\text{out}}$  is typically underestimated by a factor of  $\sim 0.8$  and  $\sim 0.9$  for the GMC with lower  $S/N$  and higher  $S/N$ , respectively. In panel (c), the corrected  $M_{\text{mol}}$  is mostly equal to the input  $M_{\text{mol}}$  for the GMC with higher  $S/N$ , but the corrected  $M_{\text{mol}}$  is typically underestimated by a factor of  $\sim 0.9$  for the GMC with lower  $S/N$ . Because about 70 per cent of the catalogued GMCs were detected with  $4 \leq S/N \leq 7$ ,  $R$  and  $M_{\text{mol}}$  may be slightly underestimated by a factor of  $\sim 0.8$  and  $\sim 0.9$ . Note that the factors of over/underestimation do not change if the GMC's minor-to-major axial ratio is set to be 0.5.

These over/underestimation can propagate to the measurements of  $M_{\text{vir}}$ ,  $\Sigma_{\text{mol}}$ ,  $\alpha_{\text{vir}}$ , and  $c$ , which are a combination of  $\sigma_v$ ,  $R$ , and  $M_{\text{mol}}$ . Thus, we recalculated the GMC properties. We corrected the catalogued  $\sigma_v$  by dividing by 1.5 if  $\sigma_v^{\text{obs}} \geq 2\sigma_{\text{ch}}$ . The catalogued  $R$  is corrected by dividing by 0.8 and 0.9 for the GMCs with lower and higher  $S/N$ . For the  $M_{\text{mol}}$ , we corrected by dividing by 0.9 for the GMCs with lower  $S/N$ . Then, we recalculated other properties based on the corrected  $\sigma_v$ ,  $R$ , and  $M_{\text{mol}}$ . Table A1 is the same as Table 3 but corrected for the over/underestimation. We find the recalculated median  $M_{\text{vir}}$ ,  $\Sigma_{\text{mol}}$ , and  $c$  become by a factor of 0.7–0.9 smaller and the correction factor is roughly comparable in the different environments. The  $\alpha_{\text{vir}}$  becomes by a factor of 0.8, 0.5, and 0.8 smaller in *bar*, *arm*, and *bar-end*, respectively. This suggests we overestimate the fraction of gravitationally unbound clouds. Based on the corrected (uncorrected) values, the number fraction is 50 per cent (58 per cent), 29 per cent (33 per cent), and 23 per cent (29 per cent) in *bar*, *arm*, and *bar-end*, respectively.

We retested the environmental variation of the GMC properties using the corrected catalogue. Table A2 shows the result of the two-sided K-S test. Comparing the Table 4,  $p$ -values do not change much. Therefore, the over/underestimation of the measurements does not influence on the discussion about the environmental variation described in Section 5.1. It is notable that  $\sim 35$  per cent and  $\sim 60$  per cent of the GMCs in M51 measured by Colombo et al. (2014) may be underestimated and overestimated by a factor of  $\sim 1.2$ . Thus, the over/underestimation seems not to influence on the discussion about the comparison with the GMCs in M51.

**Table A1.** GMC properties in the different environments of NGC 1300 corrected for the CPROPS bias.

Envir.	$\sigma v$ ( $\text{km s}^{-1}$ )	$R$ (pc)	$M_{\text{mol}}$ ( $10^5 M_{\odot}$ )	$M_{\text{vir}}$ ( $10^5 M_{\odot}$ )	$\Sigma_{\text{mol}}$ ( $M_{\odot} \text{ pc}^{-2}$ )	$\alpha_{\text{vir}}$	$c$ ( $\text{km s}^{-1} \text{ pc}^{-0.5}$ )
All	$4.0^{+1.8}_{-0.9}$	$56.4^{+12.1}_{-13.7}$	$5.7^{+4.7}_{-1.9}$	$11.0^{+12.6}_{-4.78}$	$127.8^{+45.6}_{-45.9}$	$1.1^{+1.2}_{-0.6}$	$0.6^{+0.2}_{-0.2}$
Bar	$4.8^{+1.3}_{-1.5}$	$58.4^{+22.2}_{-19.3}$	$6.1^{+2.0}_{-2.1}$	$14.6^{+8.5}_{-8.77}$	$91.7^{+64.6}_{-28.6}$	$2.0^{+0.9}_{-1.4}$	$0.7^{+0.1}_{-0.2}$
Arm	$3.7^{+1.5}_{-0.8}$	$55.0^{+10.7}_{-11.8}$	$5.5^{+4.2}_{-1.8}$	$9.8^{+6.4}_{-4.14}$	$111.4^{+55.7}_{-29.3}$	$0.9^{+1.2}_{-0.4}$	$0.6^{+0.2}_{-0.2}$
Bar-end	$3.9^{+2.6}_{-0.7}$	$57.0^{+21.4}_{-15.7}$	$9.1^{+6.4}_{-3.6}$	$14.0^{+17.9}_{-7.69}$	$143.9^{+77.8}_{-33.4}$	$1.1^{+0.6}_{-0.5}$	$0.7^{+0.2}_{-0.2}$

**Table A2.** Kolmogorov–Smirnov test for GMC properties corrected for the CPROPS bias.

Prop.	Bar versus Arm	Bar versus Bar-end	Arm versus Bar-end
$\sigma v$	$0.138 \pm 0.062(0.169)$	$0.538 \pm 0.166(0.538)$	$0.422 \pm 0.123(0.460)$
$R$	$0.746 \pm 0.100(0.914)$	$0.896 \pm 0.078(0.952)$	$0.556 \pm 0.149(0.450)$
$M_{\text{mol}}$	$0.841 \pm 0.103(0.938)$	$0.028 \pm 0.018(0.027)$	$0.013 \pm 0.007(0.006)$
$M_{\text{vir}}$	$0.571 \pm 0.199(0.438)$	$0.865 \pm 0.099(0.865)$	$0.242 \pm 0.092(0.261)$
$\Sigma_{\text{mol}}$	$0.547 \pm 0.183(0.530)$	$0.142 \pm 0.077(0.142)$	$0.093 \pm 0.055(0.139)$
$\alpha_{\text{vir}}$	$0.312 \pm 0.120(0.283)$	$0.185 \pm 0.077(0.221)$	$0.669 \pm 0.148(0.664)$
$c$	$0.409 \pm 0.092(0.409)$	$0.739 \pm 0.166(0.712)$	$0.359 \pm 0.111(0.430)$

**APPENDIX B: GMC CATALOGUE**

Table B1 presents the GMC catalogue in NGC 1300, which contains columns as follows:

- (i) Column 1: ID, GMC identification number
- (ii) Column 2: RA, GMC right ascension as measured by the intensity-weighted first moment along this direction
- (iii) Column 3: Dec., GMC declination measured as above
- (iv) Column 4:  $v_{\text{LSR}}$ , GMC central velocity as measured by the intensity-weighted first moment along the velocity axis
- (v) Column 5:  $T_{\text{peak}}$ , GMC's peak brightness temperature in K
- (vi) Column 6: S/N, GMC's peak signal-to-noise ratio
- (vii) Column 7:  $\sigma_v$ , GMC's deconvolved, extrapolated velocity dispersion in  $\text{km s}^{-1}$  with uncertainty
- (viii) Column 8:  $R$ , GMC's deconvolved, extrapolated effective radius in pc with uncertainty

(ix) Column 9:  $M_{\text{mol}}$ , GMC's mass in  $10^5 M_{\odot}$  calculated from CO luminosity and  $\alpha_{\text{CO}} = 4.4 M_{\odot} (\text{K km s}^{-1} \text{pc}^2)^{-1}$  with uncertainty

(x) Column 10:  $M_{\text{vir}}$ , GMC's mass inferred from virial theorem in  $10^5 M_{\odot}$  with uncertainty

(xi) Column 11:  $\alpha_{\text{vir}}$ , GMC's virial parameter with uncertainty

(xii) Column 12: Region where a given GMC has been identified, i.e. bar, arm, bar-end, and 'other', which represents the GMC outside the three regions

(xiii) Column 13: Flag for the measurement of radius: 0 = actual measurement of radius, 1 = upper limit

Here we show the first 10 entries of the GMC catalogue. The complete version is available in machine-readable form in the online journal.

**Table B1.** GMC catalogue.

ID	RA (J2000)	Dec. (J2000)	$v_{\text{LSR}}$ ( $\text{km s}^{-1}$ )	$T_{\text{peak}}$ (K)	S/N	$\sigma_v$ ( $\text{km s}^{-1}$ )	$R$ (pc)	$M_{\text{mol}}$ ( $10^5 M_{\odot}$ )	$M_{\text{vir}}$ ( $10^5 M_{\odot}$ )	$\alpha_{\text{vir}}$	Reg	Flag
1	3 <sup>h</sup> 19 <sup>m</sup> 35 <sup>s</sup> .56	−19°24′25″.1	1675.8	2.8	5.5	7.9 ± 4.8	43.2 ± 34.9	10.4 ± 6.4	28.3 ± 53.3	3.0 ± 4.9	Bar-end	0
2	3 <sup>h</sup> 19 <sup>m</sup> 35 <sup>s</sup> .53	−19°24′24″.6	1670.1	2.8	5.3	7.9 ± 5.2	<29.6	2.9 ± 4.1	–	–	Bar-end	1
3	3 <sup>h</sup> 19 <sup>m</sup> 35 <sup>s</sup> .53	−19°24′25″.7	1666.2	4.2	7.9	7.7 ± 2.4	77.5 ± 16.8	26.5 ± 6.9	47.9 ± 30.1	2.0 ± 1.2	Bar-end	0
4	3 <sup>h</sup> 19 <sup>m</sup> 35 <sup>s</sup> .50	−19°24′04″.8	1667.9	1.8	4.7	4.4 ± 5.1	<29.6	1.1 ± 1.3	–	–	Arm	1
5	3 <sup>h</sup> 19 <sup>m</sup> 35 <sup>s</sup> .46	−19°24′04″.3	1666.6	2.1	5.3	4.2 ± 2.6	24.7 ± 14.9	2.8 ± 1.7	4.5 ± 6.9	1.8 ± 2.2	Arm	0
6	3 <sup>h</sup> 19 <sup>m</sup> 35 <sup>s</sup> .74	−19°24′28″.2	1662.4	4.2	8.9	5.1 ± 2.0	61.1 ± 26.4	15.5 ± 11.0	16.3 ± 16.0	1.2 ± 1.2	Bar-end	0
7	3 <sup>h</sup> 19 <sup>m</sup> 35 <sup>s</sup> .72	−19°24′19″.8	1662.1	4.0	8.4	6.6 ± 2.2	56.4 ± 20.5	24.1 ± 9.5	25.7 ± 17.6	1.2 ± 0.9	Bar-end	0
8	3 <sup>h</sup> 19 <sup>m</sup> 35 <sup>s</sup> .66	−19°24′18″.6	1666.7	2.9	6.8	6.4 ± 6.4	14.4 ± 21.0	5.1 ± 4.2	6.1 ± 14.6	1.3 ± 3.3	Bar-end	0
9	3 <sup>h</sup> 19 <sup>m</sup> 35 <sup>s</sup> .73	−19°24′17″.7	1663.0	3.5	8.3	5.7 ± 3.8	35.4 ± 26.1	6.6 ± 5.4	11.8 ± 19.4	2.0 ± 2.8	Bar-end	0
10	3 <sup>h</sup> 19 <sup>m</sup> 35 <sup>s</sup> .51	−19°24′03″.7	1659.9	2.2	5.4	3.1 ± 2.3	<29.6	2.7 ± 1.0	–	–	Arm	1
–	–	–	–	–	–	–	–	–	–	–	–	–
–	–	–	–	–	–	–	–	–	–	–	–	–
–	–	–	–	–	–	–	–	–	–	–	–	–
233	3 <sup>h</sup> 19 <sup>m</sup> 36 <sup>s</sup> .59	−19°23′37″.3	1578.5	3.1	4.9	5.6 ± 2.6	<29.6	2.9 ± 1.8	–	–	Arm	1

This paper has been typeset from a  $\text{\LaTeX}$  file prepared by the author.